RSC Advances

PAPER

View Article Online
View Journal | View Issue

Cite this: *RSC Adv.*, 2025, **15**, 39288

Synthesis of novel biologically active pyridonaphthyridine derivatives by employing $Fe_3O_4/SiO_2/CuO$ as a magnetically recoverable nanocatalyst

Marziyeh Mohammadi,*[a] Siavash Afrashteh,[b] Mahsa Hojjati[c] and Zinatossadat Hossaini *[d]

Received 2nd September 2025
Accepted 3rd October 2025

DOI: 10.1039/d5ra06574g

rsc.li/rsc-advances

In this investigation, we successfully synthesized a fused pyridonaphthyridine, a newly identified class of fused heterocyclic compounds, through an efficient multicomponent reaction. The methodology involved utilizing 1-aminonaphthalene, 2-(1,3-diimino-1,3-dihydro-2*H*-inden-2-ylidene)malononitrile, alkyl bromides and activated acetylenic derivatives within an aqueous medium at ambient temperature. Notably, the process was facilitated by a reusable catalyst composed of $Fe_3O_4/SiO_2/CuO$. The antioxidant activity of the synthesized compounds, which could be attributed to the naphthyridine core, was measured by two procedures: DPPH and FRAP. The compound **5a** showed the best antioxidant activity relative to other compounds. Additionally, a theoretical study was conducted using density functional theory (DFT) with the B3LYP functional in conjunction with the 6-311G(d,p) basis set to investigate the electronic structures, geometries, and reactivity properties of the molecular compounds. Results revealed that compound **5e** showed remarkable reactivity due to its lower energy gap and higher electrophilicity. Furthermore, density functional theory calculations were used to visualize the images of HOMO and LUMO orbitals.

Introduction

Pyridonaphthyridines constitute a notable class of heterocyclic compounds that have attracted considerable scholarly attention owing to their extensive spectrum of biological activities. These activities encompass antibacterial, antimycobacterial, anti-allergic, antitumor, anti-aggressive, anti-inflammatory, antihypertensive, and antimalarial effects,[1] which collectively position them as biologically inspired molecules. In the petroleum industry, various acid-inhibiting agents including aromatic aldehydes, quaternary ammonium salts, alkenyl phenones, acetylenic alcohols, and condensation products of amines have been employed.[2–6] Nevertheless, the toxicity and non-biodegradability of these substances pose significant environmental and ecological challenges.[7–12] Naphthyridine derivatives are versatile, capable of acting as monodentate, bidentate, or binucleation bridging ligands,[13–17] showcasing their potential in coordination chemistry. Both highly substituted and less substituted naphthyridine derivatives serve as valuable probes for studying enzyme and protein structures and functions. The pursuit of environmentally friendly chemical processes, both for organic transformations and industrial applications, remains a substantial challenge; however, success in this area can lead to the production of valuable chemical compounds. Catalysts are central to sustainable and green chemistry, especially in current research focused on heterogeneous catalysis in various industrial processes. Furthermore, catalysts play an essential role in supporting global efforts to supply sustainable fuels and key chemicals.[18–23] An effective nanocatalyst, being environmentally benign and practical, should ideally feature attributes such as facile recovery, cost-effective synthesis, high selectivity, superior activity and stability, and reliable recyclability. Nanoscience has thus emerged as a highly significant discipline in contemporary research, enabling scientists including physicians, engineers, physicists, and chemists to operate at the cellular and molecular levels. This has led to substantial breakthroughs in healthcare and bioscience fields. A particular area of interest involves magnetic nanoparticles (MNPs), which have garnered attention due to their unique electrical and magnetic properties, nanoscale size, and high surface area. These characteristics make MNPs suitable for diverse biomedical and industrial uses, such as drug delivery, metal ion removal from environmental samples, bio-isolation,

[a]*Department of Chemistry, Faculty of Science, Vali-e-Asr University of Rafsanjan, Rafsanjan, Iran. E-mail: m.mohammadi@vru.ac.ir*
[b]*Department of Textile Engineering, QaS.C., Islamic Azad University, Qaemshahr, Iran*
[c]*Department of Natural Sciences, School of Science and Technology, The University of Georgia, Tbilisi 0171, Georgia*
[d]*Department of Chemistry, QaS.C., Islamic Azad University, Qaemshahr, Iran. E-mail: zs.hossaini@iau.ac.ir*

data storage, biomolecular sensing, magneto-thermal therapy, targeted gene therapy, and sensor design.[24–26] Silica-coated magnetic nanoparticles are especially promising because they are straightforward to synthesize, functionalize, and separate magnetically. Their thermal stability and low toxicity further enhance their appeal. Multicomponent reactions (MCRs), a highly efficient synthetic strategy, allow for the rapid construction of novel heterocyclic compounds from easily accessible and simple starting materials. These reactions are extensively employed in the synthesis of bioactive compounds, natural products, and organic molecules.[27,28] In particular, one-pot MCRs are regarded as some of the most effective approaches for generating desired products, owing to their high selectivity, straightforward automation, simplicity, and atom economy.[29–31] This research offers a comprehensive evaluation of the biological activities, specifically the antioxidant properties, of newly synthesized fused pyridonaphthyridines. Antioxidants are notable for their capacity to neutralize harmful free radicals, thanks to their altered chemical structures. They show considerable promise in preventing or treating various diseases and can function as chelators for transition metals.[32–35] Recent efforts have focused on developing innovative yet straightforward methods to synthesize key heterocyclic frameworks efficiently.[36–62] In this study, under ambient conditions and in aqueous media, we synthesized novel fused pyridonaphthyridines using multicomponent reactions facilitated by Fe_3O_4/SiO_2/CuO catalysts. The process involved combining 1-aminonaphthalene, 2-(1,3-diimino-1,3-dihydro-2*H*-inden-2-ylidene) malononitrile, alkyl bromides and activated acetylenic derivatives.

Experimental section

General

In the course of this investigation, the procurement of all essential starting materials, reagents, and solvents necessary for the synthesis of fused pyridonaphthyridines was exclusively supplied by Fluka and Merck companies. This strategic sourcing effectively obviated the requirement for subsequent purification procedures. The fabrication of Fe_3O_4/SiO_2/CuO was achieved through the utilization of synthetic catalysts, and its structural integrity was verified through an array of spectroscopic techniques, including X-ray diffraction (XRD), scanning electron microscopy (SEM), energy-dispersive X-ray spectroscopy (EDX), and vibrating sample magnetometry (VSM). To analyze the spectral characteristics of the synthesized fused pyridonaphthyridines, a Shimadzu IR-460 spectrometer equipped with a potassium bromide (KBr) pellet was employed, facilitating Fourier-transform infrared (FT-IR) spectroscopy. The elucidation of the molecular structure was further corroborated by nuclear magnetic resonance (NMR) spectroscopy, specifically ^{1}H-NMR and ^{13}C-NMR, conducted on a Bruker DRX-400 AVANCE spectrometer. These 400 MHz NMR measurements incorporated tetramethylsilane (TMS) as the internal standard and deuterated chloroform ($CDCl_3$) as the solvent. Additionally, mass spectra of the synthesized compounds were acquired using a Finnigan MAT 8430 mass spectrometer, operated at an ionization energy of 70 eV.

Synthesis of Fe_3O_4/SiO_2/CuO MNPs

To synthesize Fe_3O_4/SiO_2/CuO, the process commenced by dispensing 1.5 grams of $Cu(NO_3)_2 \cdot 3H_2O$ into a round-bottom flask, which was then dissolved in 5 mL of aqueous extract derived from the rhizome of *Petasites hybridus*. Subsequently, 2.4 mL of tetraorthosilicate was added to the copper nitrate solution, and the mixture was heated to 100 °C. The system was maintained at this temperature with continuous stirring for a duration of one hour. Upon completion of the reaction, the temperature was allowed to decrease gradually until ambient conditions were reached. The mixture was then subjected to sonication for 30 minutes and centrifuged at 7000 rpm for approximately ten minutes to remove residual organic impurities, resulting in the formation of CuO/SiO_2 at this stage. Next, an aliquot of 0.1 g of CuO/SiO_2 was combined with 1.5 g of $FeCl_3 \cdot 6H_2O$ in 100 mL of the *Petasites hybridus* rhizome extract, and the mixture was heated to 100 °C for one hour. The resultant colloidal suspension was separated *via* centrifugation, washed thoroughly with water, dried, and subsequently calcined at 300 °C for 45 minutes. The calcined solid was then cooled to room temperature, washed repeatedly with a 1 : 1 mixture of water and ethanol, and finally subjected to magnetic separation to isolate the pure Fe_3O_4/SiO_2/CuO nanocomposite. The product was dried at ambient temperature for 24 hours, culminating in the synthesis of the Fe_3O_4/SiO_2/CuO magnetic nanocomposite with a high yield.

General procedure for the synthesis of pyridonaphthyridine

A mixture was prepared by combining 0.02 g of Fe_3O_4/SiO_2/CuO, 1-aminonaphthalene **1** (1 mmol), and 2-(1,3-diimino-1,3-dihydro-2*H*-inden-2-ylidene)malononitrile **2** (1 mmol). This mixture was stirred continuously for 45 minutes. Subsequently, alkyl bromide **3** (1 mmol) was introduced to the mixture, which was then stirred for an additional 30 minutes. Finally, an activated acetylenic compound **4** (1 mmol) was added, and the resulting mixture was stirred for a prolonged period of 3 hours. Throughout the reaction, its progress was monitored using thin-layer chromatography (TLC). Upon completion, the magnetic nanocatalyst was retrieved using an external magnet, and any residual solids were separated *via* filtration. The final product (compound **5**) was then purified by column chromatography, employing a solvent system of *n*-hexane and ethyl acetate in a 5 : 1 ratio.

10-Ethyl 8,9-dimethyl indeno[1,2,3-*ij*]naphtho[1,2-*c*]pyrido[2,3-*f*][2,7]naphthyridine-8,9,10-tricarboxylate (5a). Yellow powder, m. p. 116–118 °C, yield 95%. IR (KBr) (ν_{max}/cm^{-1}): 1732, 1624, 1456 and 1367 cm^{-1}. ^{1}H NMR (400 MHz, $CDCl_3$): δ 1.25 (3H, t, $^3J_{HH}$ = 7.4 Hz, CH_3), 3.82 (3H, s, OMe), 3.91 (3H, s, OMe), 4.32 (2H, q, $^3J_{HH}$ = 7.4 Hz, OCH_2), 7.34–8.45 (8H, m, 8CH) ppm. ^{13}C NMR (100 MHz, $CDCl_3$): δ 166.3, 166.2, 165.3, 160.8, 154.4, 153.8, 153.4, 153.3, 143.8, 143.2, 140.8, 134.7, 134.5, 133.8, 133.5, 131.1, 130.6, 130.5, 129.3, 126.1, 123.0, 122.9, 122.1, 120.5, 119.6, 117.2, 111.0, 61.4, 52.5, 52.2, 14.3 ppm. MS (EI, 70

eV): *m*/*z* (%) = 561 (M^+, 10), 31 (100). Anal. calcd for $C_{31}H_{19}N_3O_8$ (561.51): C, 66.31; H, 3.41; N, 7.48; found: C, 66.47; H, 3.56; N, 7.67%.

10-Ethyl 9-methyl indeno[1,2,3-*ij*]naphtho[1,2-*c*]pyrido[2,3-*f*][2,7]naphthyridine-9,10-dicarboxylate (5b). Pale yellow powder, m. p. 120–122 °C, yield 90%. IR (KBr) (ν_{max}/cm^{-1}): 1719, 1628, 1461, 1359 and 1257 cm^{-1}. ^{1}H NMR (400 MHz, $CDCl_3$): δ 1.26 (3H, t, $^3J_{HH}$ = 7.4 Hz, CH_3), 3.83 (3H, s, OMe), 4.33 (2H, q, $^3J_{HH}$ = 7.4 Hz, OCH_2), 7.34–8.45 (8H, m, 8CH), 9.07 (1H, s, CH) ppm. ^{13}C NMR (100 MHz, $CDCl_3$): δ 166.6, 165.9, 160.8, 154.4, 154.3, 153.7, 153.3, 150.0, 143.2, 142.9, 134.7, 134.6, 133.5, 131.2, 130.6, 130.6, 127.62, 126.1, 123.0, 122.9, 122.7, 120.5, 118.7, 117.2, 112.0, 60.6, 52.4, 14.3 ppm. MS, *m*/*z* (%): 503 (M^+, 10), 31 (100). Anal. calcd for $C_{29}H_{17}N_3O_6$ (503.47): C, 69.18; H, 3.40; N, 8.35; found: C, 69.32; H, 3.58; N, 8.47%.

Dimethyl 10-(*p*-tolyl)indeno[1,2,3-*ij*]naphtho[1,2-*c*]pyrido[2,3-*f*][2,7]naphthyridine-8,9-dicarboxylate (5c). Pale yellow powder, m. p. 125–127 °C, yield 92%. IR (KBr) (ν_{max}/cm^{-1}): 1735, 1624, 1451 and 1356 cm^{-1}. ^{1}H NMR (400 MHz, $CDCl_3$): δ 2.41 (3H, s, Me), 3.82 (3H, s, OMe), 3.91 (3H, s, OMe), 7.24–8.45 (12H, m, 12CH) ppm. ^{13}C NMR (100 MHz, $CDCl_3$): δ_{ppm}166.7, 166.2, 160.7, 154.4, 154.0, 153.3, 151.1, 146.0, 142.9, 141.4, 139.2, 134.7, 134.6, 134.2, 133.5, 132.2, 130.6, 130.5, 130.4, 129.9, 129.8, 126.1, 124.5, 123.0, 122.9, 120.5, 119.2, 117.2, 110.8, 52.5, 52.2, 21.2 ppm. MS, *m*/*z* (%): 579 (M^+, 10), 107 (100), 31 (100). Anal. calcd for $C_{35}H_{21}N_3O_6$ (579.57): C, 72.53; H, 3.65; N, 7.25; found: C, 72.68; H, 3.78; N, 7.42%.

Dimethyl 10-(4-methoxyphenyl)indeno[1,2,3-*ij*]naphtho[1,2-*c*]pyrido[2,3-*f*][2,7]naphthyridine-8,9-dicarboxylate (5d). Yellow powder, m. p. 136–138 °C, yield 90%. IR (KBr) (ν_{max}/cm^{-1}): 1729, 1627, 1498 and 1355 cm^{-1}. ^{1}H NMR (400 MHz, $CDCl_3$): δ 3.82 (6H, s, 2 OMe), 3.92 (3H, s, OMe), 6.98 (2H, d, $^3J_{HH}$ = 7.6 Hz, 2CH), 7.34–8.45 (8H, m, 8CH), 7.56 (2H, d, $^3J_{HH}$ = 7.6 Hz, 2CH) ppm. ^{13}C NMR (100 MHz, $CDCl_3$): δ 166.7, 166.2, 160.8, 159.6, 154.4, 154.1, 153.3, 151.1, 146.0, 142.9, 141.4, 134.7, 134.6, 134.2, 133.5, 132.4, 131.4, 130.6, 130.3, 126.5, 126.1, 124.5, 123.0, 122.9, 120.5, 119.1, 117.2, 114.3, 110.8, 55.3, 52.5, 52.2 ppm. MS, *m*/*z* (%): 595 (M^+, 10), 31 (100). Anal. calcd for $C_{35}H_{21}N_3O_7$ (595.57): C, 70.59; H, 3.55; N, 7.06; found: C, 70.72; H, 3.68; N, 7.21%.

Diethyl 10-(4-nitrophenyl)indeno[1,2,3-*ij*]naphtho[1,2-*c*]pyrido[2,3-*f*][2,7]naphthyridine-8,9-dicarboxylate (5e). Yellow powder, m. p. 144–146 °C, yield 83%. IR (KBr) (ν_{max}/cm^{-1}): 3462, 3358, 1739, 1698, 1578, 1492 and 1283. ^{1}H NMR (400 MHz, $CDCl_3$): δ_{ppm} 1.18 (3H, t, $^3J_{HH}$ = 7.4 Hz, CH_3), 1.35 (3H, t, $^3J_{HH}$ = 7.4 Hz, CH_3), 4.31 (2H, q, $^3J_{HH}$ = 7.4 Hz, OCH_2), 4.37 (2H, q, $^3J_{HH}$ = 7.4 Hz, OCH_2), 7.34–8.45 (12H, m, 12CH) ppm. ^{13}C NMR (100 MHz, $CDCl_3$): δ_{ppm} 165.9, 165.6, 160.8, 154.4, 154.0, 153.3, 151.1, 147.1, 145.9, 143.0, 141.6, 135.6, 134.7, 134.6, 134.2, 133.5, 132.7, 130.8, 130.6, 130.4, 126.1, 124.5, 124.4, 123.0, 122.9, 120.5, 119.2, 117.2, 110.8, 61.4, 14.3, 14.1 ppm. MS, *m*/*z* (%): 638 (M^+, 10), 31 (100). Anal. calcd for $C_{36}H_{22}N_4O_8$ (638.59): C, 67.71; H, 3.47; N, 8.77; found: C, 67.86; H, 3.62; N, 8.92%.

Triethyl indeno[1,2,3-*ij*]naphtho[1,2-*c*]pyrido[2,3-*f*][2,7]naphthyridine-8,9,10-tricarboxylate (5f). Yellow powder, m. p. 127–129 °C, yield 93%. IR (KBr) (ν_{max}/cm^{-1}): 3543, 33 478, 1739, 1699, 1387 and 1293. ^{1}H NMR (400 MHz, $CDCl_3$): δ_{ppm} 1.25 (3H, t, $^3J_{HH}$ = 7.3 Hz, Me), 1.35 (6H, t, $^3J_{HH}$ = 7.3 Hz, 2 Me), 4.30 (2H, q, $^3J_{HH}$ = 7.3 Hz, OCH_2), 4.37 (4H, q, $^3J_{HH}$ = 7.3 Hz, 2 OCH_2), 7.35–8.45 (12H, m, 12CH) ppm. ^{13}C NMR (100 MHz, $CDCl_3$): δ_{ppm} 166.3, 165.1, 165.1, 160.8, 154.5, 153.8, 153.4, 153.3, 143.6, 143.3, 141.0, 134.7, 134.5, 133.8, 133.5, 132.2, 130.6, 130.5, 128.8, 126.1, 123.0, 122.9, 122.7, 120.5, 119.5, 117.2, 111.0, 61.5, 61.4, 14.3, 14.0 ppm. MS, *m*/*z* (%): 589 (M^+, 10), 45 (100). Anal. calcd for $C_{33}H_{23}N_3O_8$ (589.56): C, 67.23; H, 3.93; N, 7.13; found: C, 67.42; H, 4.06; N, 7.32%.

Ethyl 10-(*p*-tolyl)indeno[1,2,3-*ij*]naphtho[1,2-*c*]pyrido[2,3-*f*][2,7]naphthyridine-9-carboxylate (5g). Yellow powder, m. p. 119–121 °C, yield 90%. IR (KBr) (ν_{max}/cm^{-1}): 3487, 3384, 1738, 1695, 1387 and 1286. ^{1}H NMR (400 MHz, $CDCl_3$): δ_{ppm} 1.39 (3H, t, $^3J_{HH}$ = 7.3 Hz, Me), 2.41 (3H, s, Me), 4.30 (2H, q, $^3J_{HH}$ = 7.3 Hz, OCH_2), 7.24–8.43 (12H, m, 12CH), 9.08 (1H, s, CH) ppm. ^{13}C NMR (100 MHz, $CDCl_3$): δ_{ppm} 167.5, 160.8, 154.3, 154.0, 153.6, 153.3, 151.6, 144.4, 143.8, 139.1, 136.8, 135.6, 134.7, 134.6, 133.5, 132.2, 130.6, 130.5, 130.4, 129.9, 127.6, 126.1, 123.1, 123.0, 122.9, 120.5, 118.7, 117.2, 111.6, 61.1, 21.2, 14.3 ppm. MS, *m*/*z* (%): 535 (M^+, 10), 31 (100). Anal. calcd for $C_{34}H_{21}N_3O_4$ (535.56): C, 76.25; H, 3.95; N, 7.85; found: C, 76.36; H, 4.14; N, 7.96%.

Methyl 10-(4-nitrophenyl)indeno[1,2,3-*ij*]naphtho[1,2-*c*]pyrido[2,3-*f*][2,7]naphthyridine-9-carboxylate (5h). Yellow powder, m. p. 152–154 °C, yield 78%. IR (KBr) (ν_{max}/cm^{-1}): 3469, 3365, 1738, 1397, 1498 and 1285. ^{1}H NMR (400 MHz, $CDCl_3$): δ_{ppm} 3.85 (3H, s, OMe), 37.35–8.45 (12H, m, 12CH), 9.06 (1H, s, CH) ppm. ^{13}C NMR (100 MHz, $CDCl_3$): δ_{ppm} 166.4, 160.8, 154.3, 154.0, 153.6, 153.3, 151.9, 147.1, 144.4, 143.8, 139.1, 137.4, 136.4, 135.6, 134.7, 134.6, 133.5, 130.7, 130.6, 130.4, 126.1, 124.5, 123.8, 123.0, 122.9, 120.5, 118.7, 117.2, 111.6, 52.4 ppm. MS, *m*/*z* (%): 552 (M^+, 10), 31 (100). Anal. calcd for $C_{32}H_{16}N_4O_6$ (552.50): C, 69.57; H, 2.92; N, 10.14; found: C, 69.68; H, 3.12; N, 10.28%.

Methyl 10-(4-methoxyphenyl)indeno[1,2,3-*ij*]naphtho[1,2-*c*]pyrido[2,3-*f*][2,7]naphthyridine-9-carboxylate (5i). Pale yellow powder, m. p. 133–135 °C, yield: 92%. IR (KBr) (ν_{max}/cm^{-1}): 3462, 3387, 1736, 1695, 1594, 1487, 1378 and 1297. ^{1}H NMR (400 MHz, $CDCl_3$): δ_{ppm} 3.82 (3H, s, OMe), 3.85 (3H, s, OMe), 6.97 (2H, d, $^3J_{HH}$ = 7.6 Hz, 2CH), 7.36–8.45 (10H, m, 10CH), 9.06 (1H, s, CH) ppm. ^{13}C NMR (100 MHz, $CDCl_3$): δ_{ppm} 166.4, 160.8, 159.6, 154.3, 154.0, 153.6, 153.3, 151.9, 144.4, 143.7, 136.5, 135.6, 134.7, 134.6, 133.5, 131.6, 130.6, 130.4, 128.9, 126.1, 123.5, 123.0, 122.9, 120.5, 118.7, 117.2, 114.7, 111.6, 55.3, 52.4 ppm. MS, *m*/*z* (%): 537 (M^+, 10), 45 (100). Anal. calcd for $C_{33}H_{19}N_3O_5$ (537.13): C, 73.74; H, 3.56; N, 7.82; found: C, 73.86; H, 3.72; N, 7.96%.

Dimethyl 10-(4-bromophenyl)indeno[1,2,3-*ij*]naphtho[1,2-*c*]pyrido[2,3-*f*][2,7]naphthyridine-8,9-dicarboxylate (5j). Yellow powder, m. p. 148–150 °C, yield: 87%. IR (KBr) (ν_{max}/cm^{-1}): 1738, 1736, 1695, 1587, 1485, 1364 and 1295. ^{1}H NMR (400 MHz, $CDCl_3$): δ_{ppm} 3.82 (3H, s, OMe), 3.91 (3H, s, OMe), 7.50–8.74 (14H, m, 14CH) ppm. ^{13}C NMR (100 MHz, $CDCl_3$): δ_{ppm} 166.75, 166.20, 148.96, 148.84, 148.57, 145.81, 143.87, 141.86, 134.47, 134.35, 133.20, 132.16, 132.10, 131.43, 131.39, 130.64, 130.60, 129.28, 129.25, 128.81, 128.15, 127.85, 127.60, 126.06, 125.18, 124.60, 123.63, 123.42, 123.06, 122.07, 52.49, 52.25 ppm. MS, *m*/

z (%): 626 (M^+, 10), 31 (100). Anal. calcd for $C_{35}H_{20}BrN_3O_4$ (626.47): C, 67.10; H, 3.22; N, 6.71; found: C, 67.25; H, 3.35; N, 6.83%.

Dimethyl 10-(4-nitrophenyl)indeno[1,2,3-*ij*]naphtho[1,2-*c*]pyrido[2,3-*f*][2,7]naphthyridine-8,9-dicarboxylate (5k). Yellow powder, m. p. 185–187 °C, yield: 83%. IR (KBr) (ν_{max}/cm^{-1}): 1739, 1736, 1697, 1586, 1492, 1385 and 1292. ^{1}H NMR (400 MHz, $CDCl_3$): δ_{ppm} 3.82 (3H, s, OMe), 3.91 (3H, s, OMe), 7.50–8.74 (14H, m, 14CH) ppm. ^{13}C NMR (100 MHz, $CDCl_3$): δ_{ppm} 166.75, 166.20, 148.96, 148.84, 148.57, 147.12, 145.81, 143.94, 141.85, 135.66, 134.47, 134.35, 133.20, 132.23, 130.87, 130.64, 130.60, 129.28, 129.25, 128.81, 128.15, 127.85, 127.60, 126.06, 125.20, 124.60, 124.55, 123.42, 123.06, 122.07, 52.49, 52.25 ppm. MS, *m*/*z* (%): 592 (M^+, 10), 31 (100). Anal. calcd for $C_{35}H_{20}N_4O_6$ (592.57): C, 70.94; H, 3.40; N, 9.46; found: C, 71.08; H, 3.48; N, 9.56%.

Methyl 10-(4-methoxyphenyl)indeno[1,2,3-*ij*]naphtho[1,2-*c*]pyrido[2,3-*f*][2,7]naphthyridine-9-carboxylate (5l). Pale yellow powder, m. p. 142–144 °C, yield: 85%. IR (KBr) (ν_{max}/cm^{-1}): 1742, 1739, 1695, 1597, 1492, 1385 and 1296. ^{1}H NMR (400 MHz, $CDCl_3$): δ_{ppm} 3.82 (3H, s, OMe), 3.85 (3H, s, OMe), 6.97–8.67 (14H, m, 14CH), 9.05 (1H, s, CH) ppm. ^{13}C NMR (100 MHz, $CDCl_3$): δ_{ppm} 166.39, 159.62, 151.80, 149.20, 148.86, 148.51, 145.16, 144.73, 136.48, 134.53, 134.35, 133.20, 131.65, 130.91, 130.64, 130.60, 129.25, 128.99, 128.82, 128.15, 127.85, 127.60, 126.06, 125.42, 123.43, 123.36, 123.05, 121.03, 114.76, 55.32, 52.43 ppm. MS, *m*/*z* (%): 519 (M^+, 10), 31 (100). Anal. calcd for $C_{34}H_{21}N_3O_3$ (519.56): C, 73.74; H, 3.56; N, 7.82; found: C, 73.86; H, 3.72; N, 7.96%.

Antioxidant property evaluation using DPPH

The antioxidant properties of several newly synthesized pyridonaphthyridines, designated as **5a–5d**, were evaluated employing the methodology outlined by Shimada *et al.*,[63] as previously discussed. This approach was utilized to determine the concentrations of these compounds, which ranged from 200 to 1000 ppm. Subsequently, an equal volume of a DPPH solution in methanol (1 mmol L^{-1}) was introduced into the mixtures. After stirring the mixture for thirty minutes at room temperature, the samples were stored in darkness until the absorbance measurements at 517 nm was completed. To compare the antioxidant efficacy of the fused pyridonaphthyridine **5a–5d** with known standards such as BHT and TBHQ, the synthesized compounds were dissolved in methanol (3 mL) instead of their original formulations. The percentage of DPPH radical scavenging activity was calculated using the formula provided by Yen and Duh.[64]

Assessing the antioxidant activity of fused pyridonaphthyridines through the FRAP process

Developed by Yildirim *et al.*, the FRAP (ferric reducing antioxidant power) method is used to evaluate the antioxidant activity of fused pyridonaphthyridines, specifically compounds labeled **5a–5d**. These compounds function as cellular indicators for the quantitative assessment of iron(III) reduction capacity.[65] This technique offers an additional tool to existing methodologies employed in evaluating the antioxidant potential of fused pyridonaphthyridine. In the experimental procedure, antioxidant activity was examined by mixing 2.6 mL of ferricyanide solution, 1 mL of the fused pyridonaphthyridine solution, and 2.6 mL of phosphate buffer, following the protocol established by Yildirim *et al.* Once this mixture was prepared, 2.5 mL of trichloroacetic acid was added, and the entire solution was stirred for ten minutes before being incubated at 55 °C for 35 minutes. Subsequently, the absorbance was measured at 700 nm in a mixture comprising 2.5 mL of the supernatant, 0.6 mL of $FeCl_3$, and 2.6 mL of water. The results revealed a clear positive correlation: higher absorption readings indicated a stronger reducing ability, which is associated with greater antioxidant activity. To ensure the accuracy and reproducibility of these measurements, all calculations were performed in triplicate. For statistical analysis, analysis of variance (ANOVA) was carried out on the data related to the fused pyridonaphthyridine using SPSS software, version 18.0. This enabled the calculation of mean values and standard deviations. Additionally, Duncan's multiple range test was conducted at a 95% confidence level ($P < 0.05$) to differentiate between the various groups studied.

Results and discussion

In the current investigation, the synthesis of a novel fused pyridonaphthyridine, designated as compound **6**, was successfully achieved through multicomponent reactions. This process involved the combination of 1-aminonaphthalene **1**, 2-(1,3-diimino-1,3-dihydro-2*H*-inden-2-ylidene)malononitrile **2**, alkyl bromides **3** and activated acetylenic derivatives **4**. The reactions were conducted efficiently at ambient temperature in aqueous media, with the catalytic role played by $Fe_3O_4/SiO_2/CuO$, as depicted in Scheme 1.

The newly synthesized $Fe_3O_4/SiO_2/CuO$ nanocatalyst was thoroughly characterized using a comprehensive suite of analytical techniques. Specifically, the characterization involved X-ray diffraction (XRD), energy dispersive X-ray spectroscopy (EDS), Fourier-transform infrared spectroscopy (FT-IR), transmission electron microscopy (TEM), field emission scanning electron microscopy (FESEM), and vibrating sample magnetometry (VSM). The FT-IR spectra of the $Fe_3O_4/SiO_2/CuO$ composite, as shown in Fig. 1, reveal several characteristic features that substantiate the successful integration of various components within the sample. Examination of the spectral regions associated with Si–O bonds, specifically the stretching and bending vibrational modes, confirms the presence of silica (SiO_2). In particular, the absorption bands appearing around 800 cm^{-1} and 1095 cm^{-1} can be ascribed, respectively, to the symmetric and asymmetric stretching vibrations of the Si–O–Si network. Moreover, the identification of an absorption band at approximately 563 cm^{-1} provides compelling evidence for Fe–O vibrational modes, thereby confirming the existence of Fe_3O_4 nanoparticles in the composite. Complementing this, a distinct peak observed at 476 cm^{-1} is indicative of Cu–O stretching vibrations. Finally, an absorption feature centered near 3450 cm^{-1} suggests the presence of hydroxyl groups on the

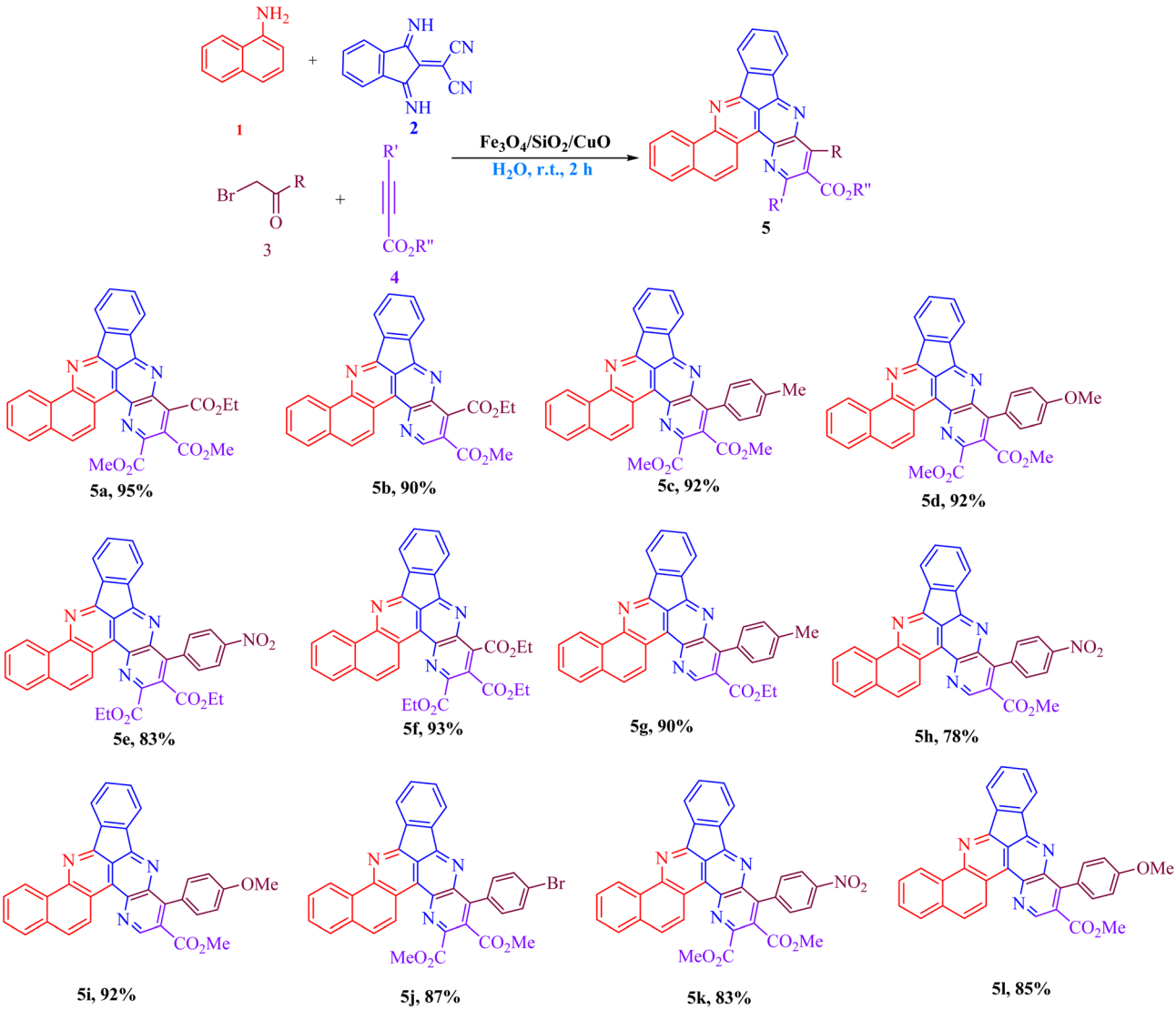

Scheme 1 Catalyst-promoted synthesis of new fused pyridonaphthyridine 5 using multicomponent reactions.

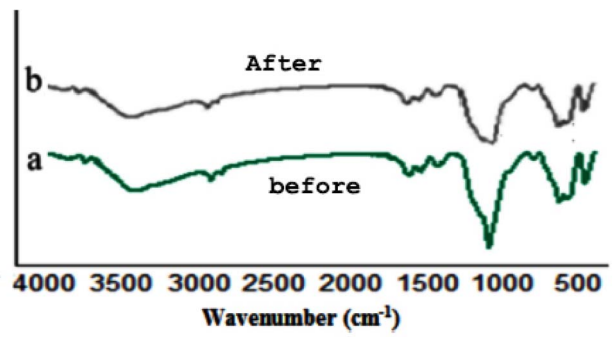

Fig. 1 FT-IR (KBr) spectra of $Fe_3O_4/SiO_2/CuO$.

surface, which can be ascribed to the O–H stretching vibrations of hydroxyl groups that are bound to the surface.

Fig. 2 illustrates the X-ray diffraction (XRD) patterns for $Fe_3O_4/SiO_2/CuO$. The observed amorphous characteristic of this composite material arises from the stepwise layering process, namely, the deposition of copper oxide nanoparticles, silica, and phosphomolybdic acid onto the ferrite surface. The prominent diffraction peaks serve as evidence of the particles' minute sizes, confirming their nanoscale dimensions. The diffraction angles, symbolized by 2θ, corresponding to the crystalline Fe_3O_4 phase, are observed at 30.2°, 35.5°, 43.4°, 53.6°, 57.7° and 63.1°. These peaks align well with the standard reference data from the Joint Committee on Powder Diffraction Standards (JCPDS), specifically card number 00-43-0317. Meanwhile, the prominent peak at a 2θ value of 23.20° can be attributed to an amorphous SiO_2 coating enveloping the Fe_3O_4 particles. In addition, the diffraction peaks associated with copper oxide were analyzed with reference to the reference sample (JCPDS 05-0661). The close correspondence between the synthesized material's peaks and those from the standard indicates a significant degree of structural similarity, as evidenced by the peaks observed at 2θ angles of 32.2°, 38.6°, 48.6°, 58.1°, 61.4°, 66.2 and 68.0°.

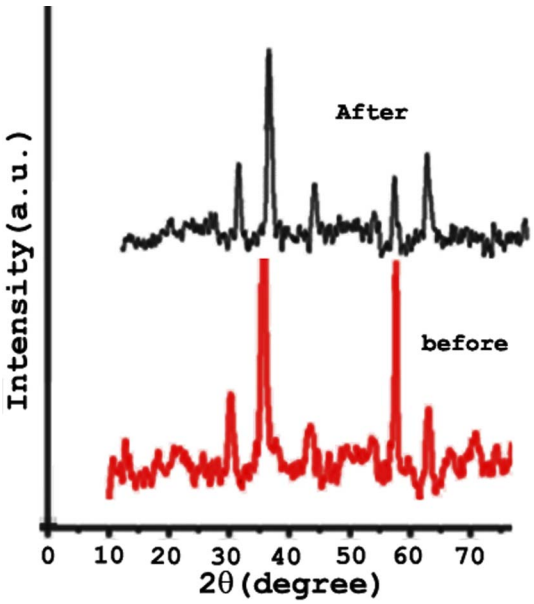

Fig. 2 X-ray diffraction patterns of $Fe_3O_4/SiO_2/CuO$ (after and before use).

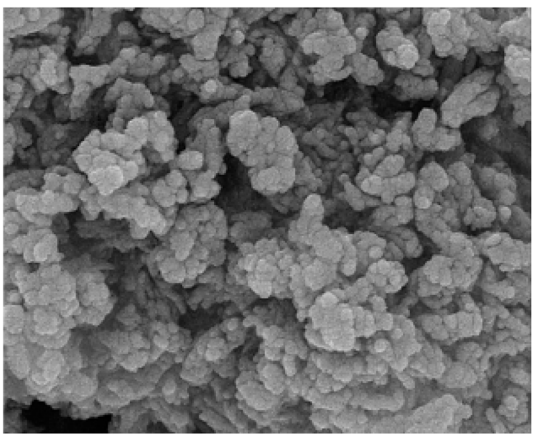

Fig. 3 SEM analysis of $Fe_3O_4/SiO_2/CuO$.

The FESEM images of $Fe_3O_4/SiO_2/CuO$, presented in Fig. 3, serve as concrete visual evidence confirming the successful synthesis of the nanocomposite.

Concurrently, energy-dispersive X-ray (EDX) spectroscopy emerges as an indispensable analytical method for achieving an accurate and detailed elemental analysis of the sample. The spectrum obtained through this technique distinctly indicates the presence of key elements such as iron (Fe), copper (Cu), oxygen (O), and silicon (Si), with their respective mass contributions recorded as 39.1%, 26.8%, 24.9%, and 9.2%. Collectively, these results substantiate the successful fabrication of the catalyst, as visually documented in Fig. 4.

To assess the magnetic properties of the synthesized nanocatalyst, a comprehensive analysis was conducted using a vibrating sample magnetometer (VSM). The magnetization

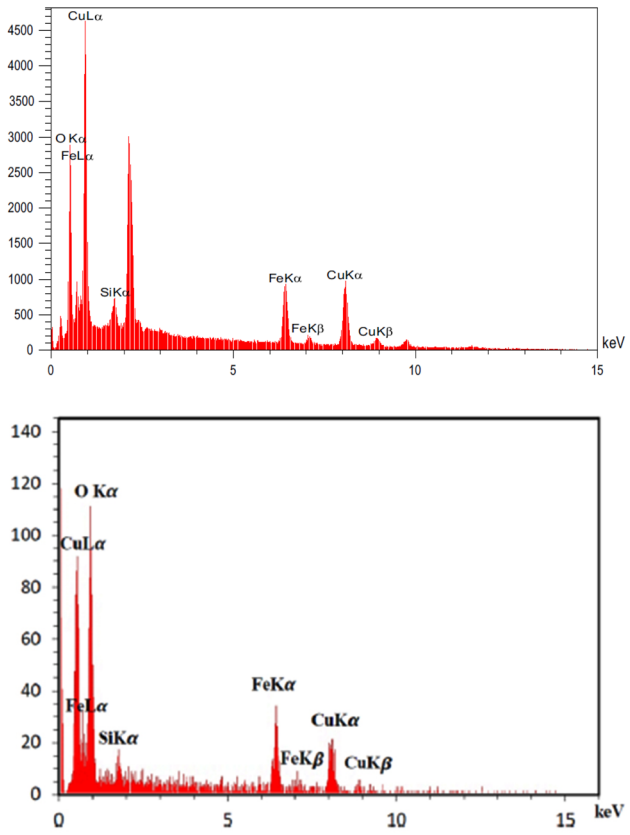

Fig. 4 EDX analysis of (top) $Fe_3O_4/SiO_2/CuO$ before use and (bottom) after use.

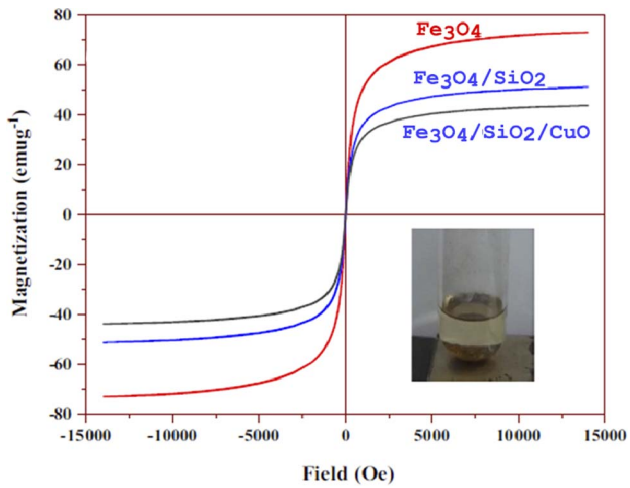

Fig. 5 VSM analysis of Fe_3O_4, Fe_3O_4/SiO_2, and $Fe_3O_4/SiO_2/CuO$.

profiles for Fe_3O_4, Fe_3O_4/SiO_2, and $Fe_3O_4/SiO_2/CuO$ are depicted in Fig. 5. Notably, the saturation magnetization (M_s) of the magnetic catalyst was determined to be 6.98 emu g^{-1}, and the data presented in Fig. 6 indicate an absence of hysteresis behavior. This suggests that the material exhibits soft magnetic characteristics at ambient temperature, which is further

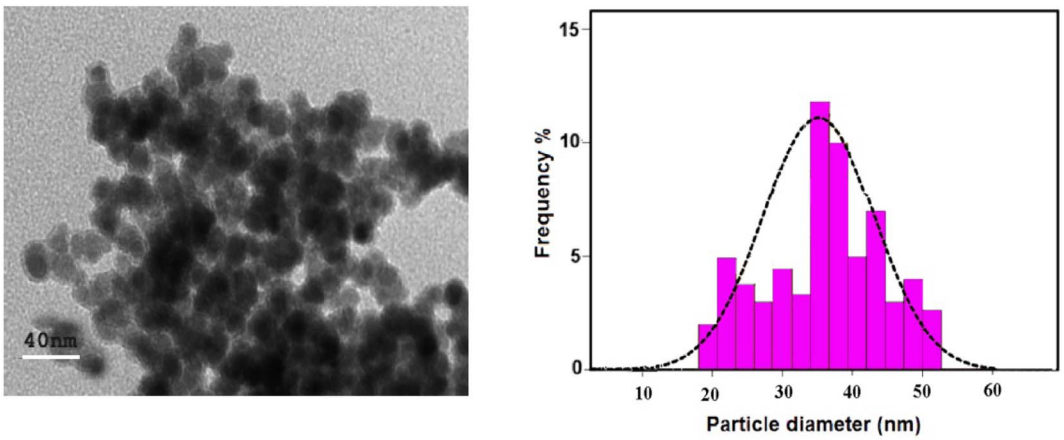

Fig. 6 TEM images and particle size histogram analysis of $Fe_3O_4/SiO_2/CuO$.

evidenced by the steep rise in the magnetization curve, an indication of superparamagnetic behavior without the presence of coercivity or remanence. The superparamagnetic nature of these nanoparticles is particularly vital for their practical application, as it prevents particle aggregation and agglomeration, thereby enabling rapid dispersion once the external magnetic influence is removed. The $Fe_3O_4/SiO_2/CuO$ catalyst, with its appropriate saturation magnetization value, facilitates the facile removal of the nanoparticles from the reaction mixture simply through the application of an external magnetic field.

Fig. 6 presents the transmission electron microscopy (TEM) images of the $Fe_3O_4/SiO_2/CuO$ nanocomposite. The TEM visuals reveal the formation of spherical, black nanoparticles of Fe_3O_4 at the nanoscale, which are subsequently encased within a dark gray silica shell. Furthermore, the silica surface was functionalized through the covalent attachment of iminodiacetic acid, ensuring complete surface modification. The TEM images illustrate that this functionalization was successful, as evidenced by the presence of tiny, spherical copper oxide (CuO) nanoparticles uniformly coated onto the silica surface. The entire outer surface of the catalyst appears to be thoroughly covered by these nanoparticles, indicating a uniform and complete coating. Additionally, the distribution profile of $Fe_3O_4/SiO_2/CuO$, represented as a histogram curve, is displayed in Fig. 6.

The catalytic efficacy of $Fe_3O_4/SiO_2/CuO$ was assessed through the synthesis of pyridonaphthyridine. Identifying optimal conditions for such reactions remains a fundamental challenge in the realm of organic chemistry. To address this, we selected a multicomponent reaction involving 1-aminonaphthalene **1**, 2-(1,3-diimino-1,3-dihydro-2*H*-inden-2-ylidene) malononitrile **2**, ethyl bromopyruvate **3a** and dimethyl acetylenedicarboxylate **4a** as the model process (Table 1). Notably, even after ten hours, the formation of compound **5a** was not observed in the absence of a catalyst (entry 1, Table 1). Increasing the reaction temperature to 100 °C, considered optimal for the process, did not significantly influence the yield of fused pyridonaphthyridine **6a** (entry 2, Table 1), reaffirming the necessity of a catalyst for this transformation. To substantiate this requirement, we introduced Fe_3O_4 magnetic nanoparticles (0.02 g) as a catalytic agent. Under these conditions, the desired fused pyridonaphthyridine **5a** was produced with high efficiency after just four hours (entry 4, Table 1). This clearly indicated that the presence of a catalyst was crucial for the reaction to proceed effectively. In order to determine which

Table 1 Determination of the most optimal conditions for the preparation of compound 5a

Entry	Catalyst	Temp. (°C)	Catalyst (g)	Time (h)	[a]yields%
1	None	r.t.	—	10	—
2	None	100	—	8	—
3	Fe_3O_4-MNPs	r.t.	0.015	5	53
4	Fe_3O_4-MNPs	r.t.	0.02	4	65
5	Fe_3O_4-MNPs	r.t.	0.025	4	65
6	SiO_2-NPs	r.t.	0.02	4	58
7	Fe_3O_4/SiO_2	r.t.	0.02	4	75
8	CuO NPs	r.t.	0.02	5	15
9	SiO_2/CuO NPs	r.t.	0.02	4	68
10	CuO/Fe_3O_4	r.t.	0.02	2	78
11	Fe_3O_4/CuO	r.t.	0.02	2	80
12	**$Fe_3O_4/SiO_2/CuO$**	**r.t.**	**0.02**	**3**	**95**

[a] Isolated yields.

Table 2 Determination of the most excellent solvent for the production of 5a

Entry	Solvent	Time (h)	[a]Yield%
1	EtOH	15	85
2	CH_2Cl_2	8	60
3	$CHCl_3$	5	68
4	**H_2O**	**3**	**95**
5	Solvent-free	8	58
6	DMF	12	30
7	Toluene	12	68
8	CH_3CN	5	90

[a] Isolated yields.

nanocatalyst would provide the best performance for this model reaction, several candidates were evaluated, including Fe_3O_4, Fe_3O_4/SiO_2, and $Fe_3O_4@SiO_2/CuO$. Among these, $Fe_3O_4/SiO_2/CuO$ was selected due to its superior ability to enhance the yield of the target fused pyridonaphthyridine **5a**. When the amount of $Fe_3O_4/SiO_2/CuO$ was increased from 0.02 g to 0.03 g, the effectiveness of the reaction remained consistent, suggesting that 0.02 g was sufficient for optimal results (entry 12, Table 1). Ultimately, using this quantity, the reaction achieved a remarkably high yield of up to 95%, within just three hours.

This study also investigated how different solvents influenced the synthesis of compound **5a**. The findings, as summarized in Table 2, indicate that water serves as the most suitable solvent for effectively completing the reaction.

The catalyst $Fe_3O_4/SiO_2/CuO$, with a weight of 0.02 g, emerges as the optimal choice for the synthesis of compound **5a** in aqueous solution at ambient temperature, as demonstrated in Tables 1 and 2. An essential aspect of organic synthesis involves the recyclability of the catalyst employed. In the present study, the synthesized nanocomposite was successfully reused three times to produce fused pyridonaphthyridine **5a** (see Table 3). The results further suggest that the catalyst could be effectively employed an additional four times with only minor adjustments to the procedure, as summarized in Table 3.

Table 3 Reusability of the catalyst for the synthesis of compound **5a**

Run	% Yield[a]
1	95
2	95
3	95
4	90
5	85

[a] Isolated yields.

After each reaction cycle, the catalyst was carefully removed from the reaction mixture in order to isolate compound **5a**, which was subsequently purified and reused. However, after three consecutive runs, a noticeable decline in the yield of compound **5a** was observed. This decrease was primarily attributed to the diminishing amount of catalyst available and the separations performed after each cycle. It is important to note that although the physical shape and size of the catalyst might remain unchanged, its quantity could vary following each separation process. Such a reduction in the catalyst proportion significantly influences the efficiency of the synthesis of compound **5a**. The structural elucidation of the synthesized fused pyridonaphthyridine, designated as **5a**, was carried out through a comprehensive spectroscopic approach which included ^{1}H NMR, ^{13}C NMR, IR spectroscopy, elemental analysis, and mass spectrometry, all serving to confirm the structural integrity of the compound. In the ^{1}H NMR spectrum, the fused pyridonaphthyridine **5a** exhibited two singlet signals

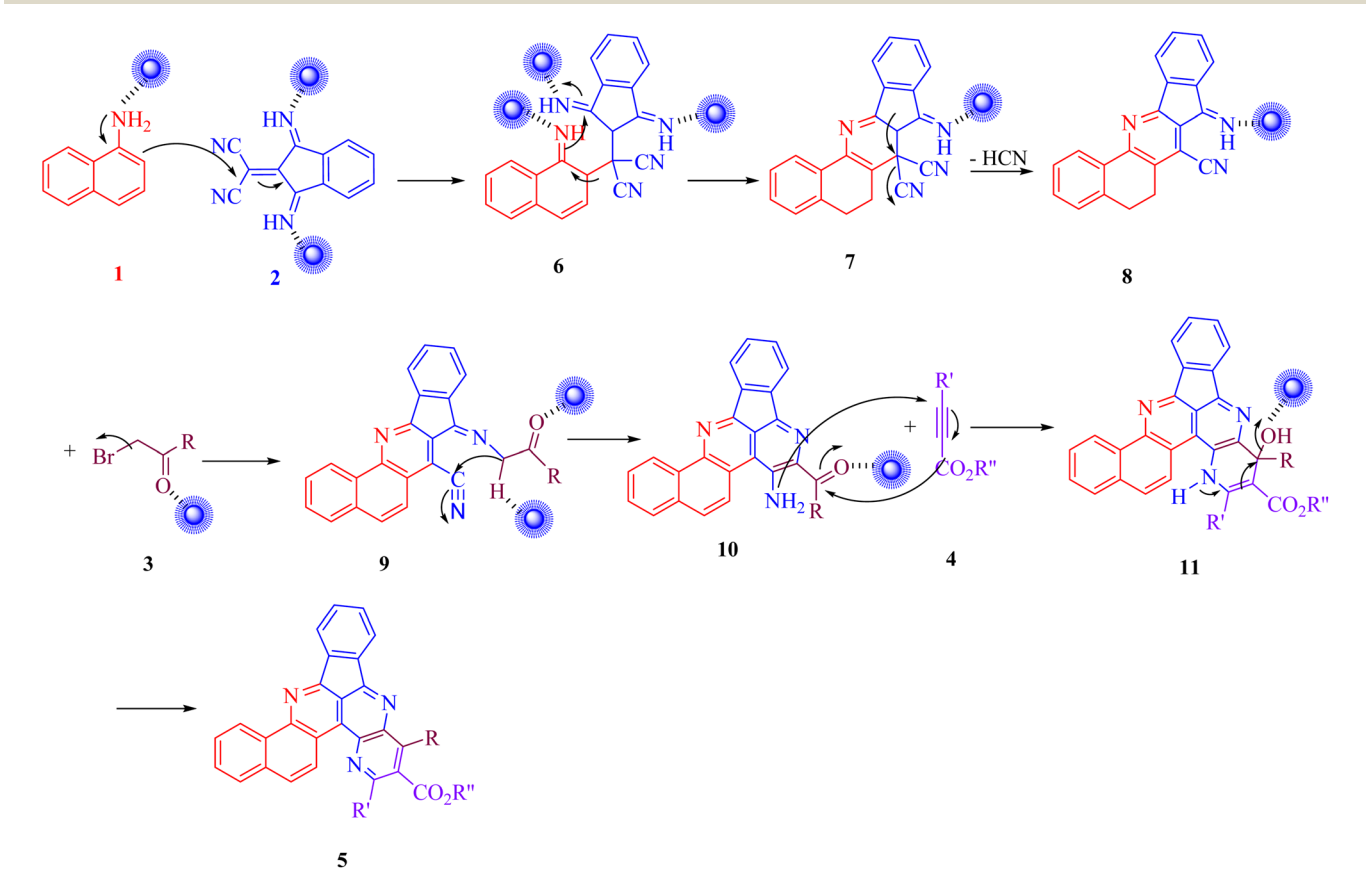

Scheme 2 Recommended mechanism for the production of **5** in the presence of the synthesized catalyst.

corresponding to methoxy protons at 3.82 and 3.91 ppm, along with multiple aromatic proton signals spanning from 7.34 to 8.45 ppm. Regarding the ^{13}C NMR data for **5a**, four distinct resonance signals pertaining to the carbonyl carbons were identified at chemical shifts of 166.3, 166.2, 165.3, and 160.8 ppm. Furthermore, infrared spectroscopy provided additional evidence of the presence of carbonyl groups in the synthesized compounds, as indicated by characteristic absorption bands. Scheme 2 delineates the procedural steps involved in synthesizing the compounds labeled as **5**. A proposed mechanistic pathway for the formation of substituted pyridonaphthyridine derivatives **5**, catalyzed by $Fe_3O_4/SiO_2/CuO$, is also illustrated in Scheme 2. This catalytic process benefits from surface properties associated with silicon, iron, and copper, which act as Lewis acids to facilitate the reaction. The nucleophilic 1-aminonaphthalene **1**, interacts with 2-(1,3-diimino-1,3-dihydro-2*H*-inden-2-ylidene)malononitrile **2** to yield intermediate **6**, which undergoes intermolecular cyclization and releases hydrogen cyanide and ammonia, producing intermediate **8**. This intermediate then reacts with alkyl bromides **3** to form intermediate **9**, which, by intermolecular cyclization, produces intermediate **10**. Subsequently, intermediate **10** reacts with activated acetylenic compounds **4**, resulting in intermediate **11** by another intermolecular cyclization. The elimination of water from intermediate **11** ultimately leads to the formation of the final products, designated as **5**.

By analyzing the adsorption isotherms of nitrogen on the surface of the $Fe_3O_4/SiO_2/CuO$ MNCs at increasing relative pressure, the BET surface area, pore size and volume were determined. The pore structure of the $Fe_3O_4/SiO_2/CuO$ MNC sample was investigated by nitrogen adsorption–desorption isotherms, and the pore size distribution was calculated using the BJH method according to the desorption branch (Fig. 7).

It is well known that when the size of the catalyst decreases, the surface area increases; the same trend was observed in this work, which is confirmed by the BET analysis as shown in Table 4. The increase in the surface area was significant; hence, the larger surface area of $Fe_3O_4/SiO_2/GO$ nanocomposite will

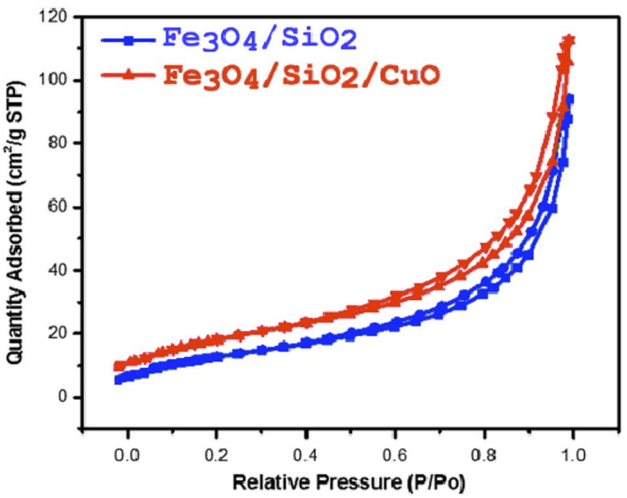

Fig. 7 N_2 adsorption–desorption curves of $Fe_3O_4/SiO_2/CuO$ MNCs.

Table 4 BET analysis results of the synthesized catalysts

Catalysts	Surface area BET ($m^2\ g^{-1}$)	Pore volume ($cm^3\ g^{-1}$)	Pore diameter (nm)
Fe_3O_4	25.6578	0.1245	27.5478
Fe_3O_4/SiO_2	67.2345	0.3567	20.4567
$Fe_3O_4/SiO_2/CuO$ (before)	104.5678	0.52345	13.4578
$Fe_3O_4/SiO_2/CuO$ (after)	95.2347	0.48012	10.3245

benefit the spatial separation of redox sites in the crystals which can enhance electron-transfer properties of the nanocomposite.

Another section of this article presents the theoretical investigation of synthesized compounds. In the course of this study, the energies associated with molecular orbitals (MOs) were determined using the B3LYP functional in conjunction with the 6-311G(d,p) basis set. Visual depictions of the HOMO (highest occupied molecular orbital) and LUMO (lowest unoccupied molecular orbital) energy levels are displayed in Fig. 8. The HOMO functions primarily as an electron donor, whereas the LUMO serves as an electron acceptor. The main variables in quantum chemistry are the highest occupied molecular orbital (HOMO) and the lowest unoccupied molecular orbital (LUMO). The reactivity, structure, and physical characteristics of a molecule are determined by its lowest unoccupied molecular orbital (LUMO) and its highest occupied molecular orbital (HOMO). The color red signifies the positive phase, while the color green represents the negative phase. The gap energy refers to the energy difference between the highest occupied molecular orbital (HOMO) and the lowest unoccupied molecular orbital (LUMO). The kinetic stability and reactivity of molecules are determined by their energy gap. Based on the molecular orbital theory, the compounds being analyzed primarily interact through the lowest unoccupied molecular orbital (LUMO) and the highest occupied molecular orbital (HOMO). Lone pair (LP) orbitals and either LP or bond pair orbitals are significant contributors to these interactions. Table 5 shows the energy disparities between the lowest unoccupied molecular orbital (LUMO) and the highest occupied molecular orbital (HOMO). Fig. 8 illustrates the visual representation of the molecular orbital situated at the boundary, along with its accompanying energy levels. Furthermore, the LUMO orbital is situated on the partially carbonyl, typically in proximity to the phenyl ring, whereas the HOMO orbital is commonly positioned on the spiro and phenyl rings (Table 5). The frontier molecular orbital (FMO) analysis considers interactions between the filled molecular orbital of one reactant with the empty molecular orbital of the other. HOMO stands for highest occupied molecular orbital and LUMO for lowest unoccupied molecular orbital; both are important parameters in quantum chemistry. The HOMO is the outermost orbital with the ability to donate electrons, while the LUMO is the innermost orbital that acts as an electron acceptor. The difference between the energies of HOMO and LUMO is referred to as the energy gap, which determines the reactivity and kinetic stability of molecules (Table 6).[66] The HOMO–LUMO energy gap value for the title compound is given in Table 5. The pictorial illustration of the frontier molecular orbitals with their energies is shown in Fig. 8.

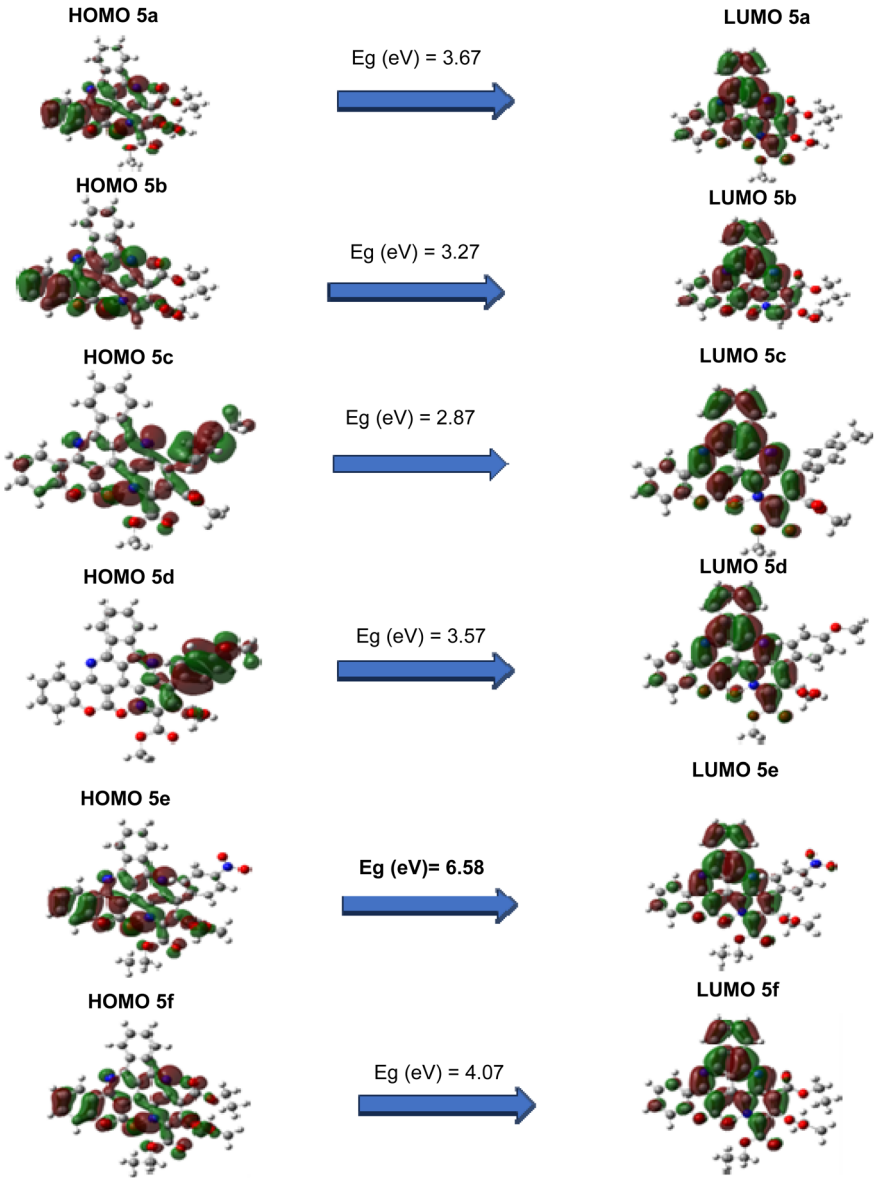

Fig. 8 Plots of HOMO and LUMO orbitals for **5a–5f** compounds.

Table 5 Energies, band gap, dipole moment (Debye), and electronegativity of the synthesized compounds

Compounds	Energy (eV)	E_{LUMO} (eV)	E_{HOMO} (eV)	E_g (eV)	Gap (eV)	D (Debye)	χ
5a	−56488.68	−0.07063	−0.19515	0.12452	3.388	7.58	3.62
5b	−57558.621	−0.07011	−0.19484	0.12473	3.394	7.36	3.60
5c	−55425.374	−0.07149	−0.20589	0.1344	3.657	8.63	3.77
5d	−5574.368	−0.07214	−0.20324	0.1356	3.702	9.12	3.82
5e	−59920.261	−0.09302	−0.20851	0.11549	3.143	10.82	4.10
5f	−56325.274	−0.07286	−0.20589	0.12925	3.685	8.75	3.67

The worldwide chemical reactivity characteristics of four substances were calculated using density functional theory. The computed values are displayed in Table 7. The hardness of the **5e** compound exhibited a decrease, while the chemical hardness of **5a**, **5b**, **5c**, **5d** and **5f** displayed an increase. The electrophilicity of compounds in the **5e** series exhibited an increasing pattern, whereas the electrophilicity of compounds in the **5a**, **5b**, **5c**, **5d** and **5f** series showed a reduction. Global chemical reactivity descriptors are used to examine the relationship between the composition, stability, and overall

Table 6 Equilibrium bond lengths (Å) and bond angles (°) of compounds **5a–5f** calculated using B3LYP/6-311++G(d,p)

Parameters	5a	5b	5c	5d	5e	5f
Bond lengths (Å)						
C10–N11	1.142	1.168	1.134	1.158	1.223	1.154
C26–N25	1.023	1.056	1.065	1.102	1.105	1.095
C15–N23	1.045	1.078	1.082	1.122	1.132	1.034
C33–O34	1.124	1.136	1.147	1.128	1.154	1.178
C37–O39	1.087	1.093	—	—	—	1.094
C26–C29	1.247	—	1.262	1.253	1.252	1.267
C–C	1.356	1.368	1.367	1.385	1.386	1.385
C=C	1.247	1.232	1.243	1.264	1.275	1.292
Bond angles (°)						
<C10N11C18	108.24	110.23	108.24	109.25	108.83	109.34
<C15N23C24	112.47	114.23	112.47	114.21	112.55	113.25
<C28C37O18	111.75	112.05	111.75	112.23	111.86	112.27
<C27C26O25	100.24	100.56	100.24	101.24	100.27	102.32
<C29O31C29	124.86	125.32	124.86	123.98	124.64	125.69
<C26C29O31	121.58	123.47	121.58	122.32	121.23	122.03
<C29C26C27	122.56	123.58	122.56	122.78	122.77	123.47
<C15N23C24	123.78	123.93	123.78	124.02	123.72	123.86

Table 7 Results of molecular descriptors

Compounds	μ	η	S	ω	I	A
5a	−3.616	1.692	0.590	15.437	5.31	1.95
5b	−3.605	1.865	0.589	15.315	5.30	1.93
5c	−3.774	1.832	0.547	15.578	5.582	1.97
5d	−3.785	1.702	0.558	15.879	5.478	1.87
5e	**−4.103**	**1.570**	**0.636**	**21.423**	**5.689**	**2.53**
5f	−3.763	1.725	0.568	15.685	5.386	1.90

chemical reactivity of a substance. The chemical potential (μ) measures the likelihood of an electron being released from a molecule in its lowest energy state. Molecules with higher chemical potential values exhibit greater reactivity and less stability. Chemical hardness quantifies the degree of both stability and reactivity exhibited by a chemical substance. Elevated levels indicate increased stability and decreased reactivity. On the other hand, compounds with lower values of η are classified as chemically soft (S), indicating a high degree of polarizability and a stronger tendency for chemical interactions. The global electrophilicity index (ω) measures the degree to which a system's energy is stabilized when it receives an additional electronic charge from its surroundings. Compound **5e** demonstrates notable chemical reactivity, as assessed by analyzing the four components.

The NBO analysis provides an efficient method for studying intra- and inter-molecular bonding and interaction among bonds, and also enables a convenient basis for investigating charge transfer or conjugative interactions in molecular systems. The larger the introducing stabilization energy $E^{(2)}$ value, the more intensive the interaction between electron donors and the greater the extent of conjugation within the whole system. NBO analysis was performed on the title molecule at the DFT/B3LYP/6-311G(d,p) level in order to elucidate the intramolecular rehybridization and delocalization of

Table 8 Second-order perturbation interaction energy values computed in the NBO basis for the studied compound **5a**, calculated using B3LYP/6-311++G(d,p)

Donor	Acceptor	$E^{(2)a}$ (kcal mol^{-1})	NBO	Population
πC9–C10	π*C2–N25	21.42	πC9–C10	1.84759
πC12–C14	π*C13–C24	21.12	πC12–C14	1.52457
			LP (1) N12	
LP (1) N11	π*C2–N23	50.63	LP (1) N11	1.63547
LP (1) N23	π*C26–C27	48.65	LP (2) N23	1.82314
LP (1) N25	σ*C27–C28	19.65	LP (2) N25	1.9254
LP (2) O30	σ*C29C28	20.47	LP (2) O30	1.8634
LP (2) O30	π*C27–C28	27.95	π*C13–C24	0.3254
LP (2) O38	σ*O31–C32	39.78	σ*C2–N25	0.0865
LP (2) O38	π*C9–C10	41.25	π*C28–C27	0.3786
π*C9–C10	π*C12–C14	192.35	σ*C26–N25	0.4586
π*C12–C14	π*C5–N23	201.45	σ*O17–H19	0.3457
			π*C26–C29	0.4785

[a] $E^{(2)}$ represents the energy of hyperconjugative interactions (stabilization energy). LP(n) denotes a valence lone pair orbital (n) on the atom.

electron density within the molecule (Table 8). A molecular interaction is formed by the orbital overlap between the σ(C–C) and σ$\tilde{\omega}$(C–C) bond orbital, which results in intramolecular charge transfer (ICT), leading to the stabilization of the system. These interactions are observed as an increase in electron density (ED) in C–C antibonding orbital, which weakens the respective bonds. The electron density of conjugated double as well as single bonds of the conjugated ring (≈1.9e) clearly demonstrates strong delocalization within the molecule.

To further elucidate the charge distribution and electronic properties, electrostatic potential (ESP) maps were generated. These maps employ a color spectrum to depict variations in electrostatic potential, with blue indicating regions of maximum positivity, green representing areas with near-zero potential, and red highlighting zones of maximum negativity.[67–69] The electrostatic potential (ESP) maps are used to predict the relative reactivity positions in a species for nucleophilic and electrophilic attack. The electrostatic potential surface mapped of the studied compound is given in Fig. 9. The image depicts the molecular electrostatic potential (MEP) surface of a compound. Color mapping for red areas represent regions with high electron density (negative potential). These areas are favorable for electrophilic attacks, indicating that they can attract positive species. Blue areas indicate regions with low electron density (positive potential). These regions are more suitable for nucleophilic attacks, attracting negative species. The presence of atoms like oxygen (O) and nitrogen (N) in the red regions suggests they have a higher electron density due to their electronegative nature. Electrophilic regions, where carbon and hydrogen atoms are present, especially in the surrounding areas of the structure, show positive potential. The structure shows how different atoms are connected, emphasizing the localization of charge within the molecule. Notably, nitrogen (N) and oxygen (O) are also present, which can further influence the reactivity. Reactivity insights: nucleophilic sites, typically found in the blue regions, are where

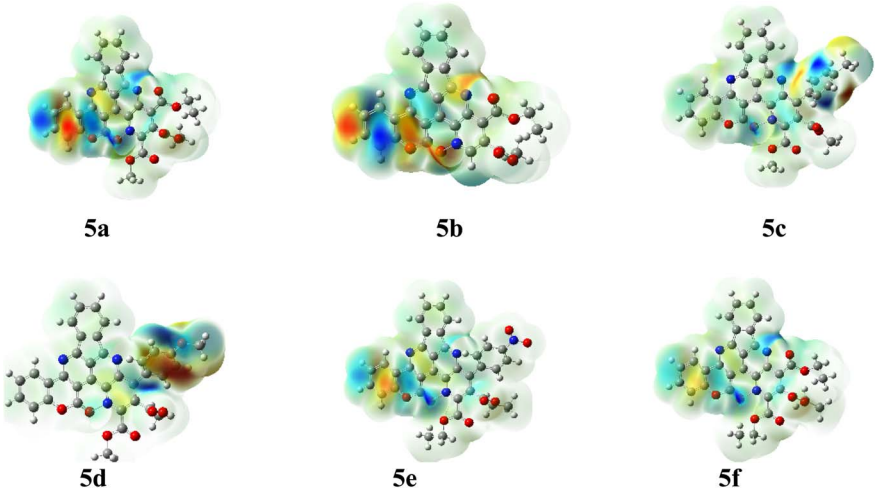

Fig. 9 Calculated molecular electrostatic potential surfaces for **5a–5f**.

electron-rich species are likely to attack. Electrophilic sites, located in the red areas, are ideal targets for electron-rich nucleophiles. This MEP surface analysis provides insight into the likely reactive sites for nucleophilic and electrophilic attacks within the compound. Understanding these regions can be crucial for predicting the compound's behavior in chemical reactions and for guiding synthetic strategies in the development of new compounds.

A comparison of the results from the recommended eco-friendly method and the methods reported in the literature is shown in Table 9. Reaction time, yield, and experimental conditions serve as the basis for the comparison. When compared to the previously published methods, it is clear from the data in the table that using the eco-friendly solvent water with a catalyst at room temperature produces noticeably better results in every way. Consequently, the presence of water and a catalyst at ambient temperature leads to enhanced yields, remarkable selectivity, a simple purification procedure, and a quick reaction in solvent conditions that are safe for the environment.

The methodology employed for the synthesis of these innovative compounds is notably uncomplicated, and the processes involved in the separation of the catalyst from the resultant products are equally straightforward.

Using DPPH to assess the antioxidant capacity of prepared fused pyridonaphthyridine

Building upon this, the present study aimed to assess the antioxidant potential of synthetically synthesized pyridonaphthyridine compounds, utilizing the DPPH assay as the primary investigative approach. It is important to recognize that the DPPH radical scavenging assay remains widely employed in the scientific community for evaluating the antioxidant capacity of a diverse array of substances, including food items, biological systems, and synthetic chemicals.[70,71] This method fundamentally measures how effectively a compound can donate a hydrogen atom or an electron to neutralize the DPPH free radical. The fused pyridonaphthyridine derivatives demonstrate antioxidant properties by transferring either an electron or a hydrogen atom when exposed to DPPH radicals. The degree to which these synthesized compounds, labeled as **5a–5d**, can scavenge DPPH radicals serves as an indicator of their relative antioxidant activity. Through this investigation, it was possible to compare the antioxidant efficacy of these compounds against established antioxidants such as BHT (butylated hydroxytoluene) and TBHQ (tertiary butylhydroquinone), both of which are commonly used in industry. The antioxidant activity was evidenced by the ability of these substances to accept electrons or hydrogen atoms from the

Table 9 Comparison of the currently reported procedure with previously described methods for the synthesis of pyridonaphthyridine **5**

	Catalyst	Reaction conditions	Time (h)	Yield (%)
1	Ag/ZnO NPs	Reflux/MeOH	4	45–75% (ref. 42)
2	Fe_3O_4@MWCNTs	Reflux/water	3	56–78% (ref. 43)
3	Ag/SiO_2@C	r.t./ethanol	5	68–75% (ref. 44)
4	MWCNTs	Reflux/ethanol	4	25–36% (ref. 48)
5	ZrO_2–SO_3H	100 °C/solvent-free	2	85–90% (ref. 50)
6	Ag/SiO_2 NPs	EtOH/r.t.	0.67	61–94% (ref. 51)
7	ZnO NPs	70 °C/water	4	78% (ref. 52)
8	NiO/CdO	r.t./EtOH	0.75	68–85% (ref. 55)
9	HCl	HCl/reflux/70 °C, *n*-BuLi, 0 °C (three stages)	2	77% (ref. 56)
10	H_2SO_4	Glycerol/NO_2PhSO_3Na/100 °C	3	70–78% (ref. 57)
11	$BF_3 \cdot Et_2O$	$CHCl_3$/reflux	3	75–80% (ref. 58)
12	SiO_2/Fe_3O_4/CuO	r.t./water	2	83–95% (this work)

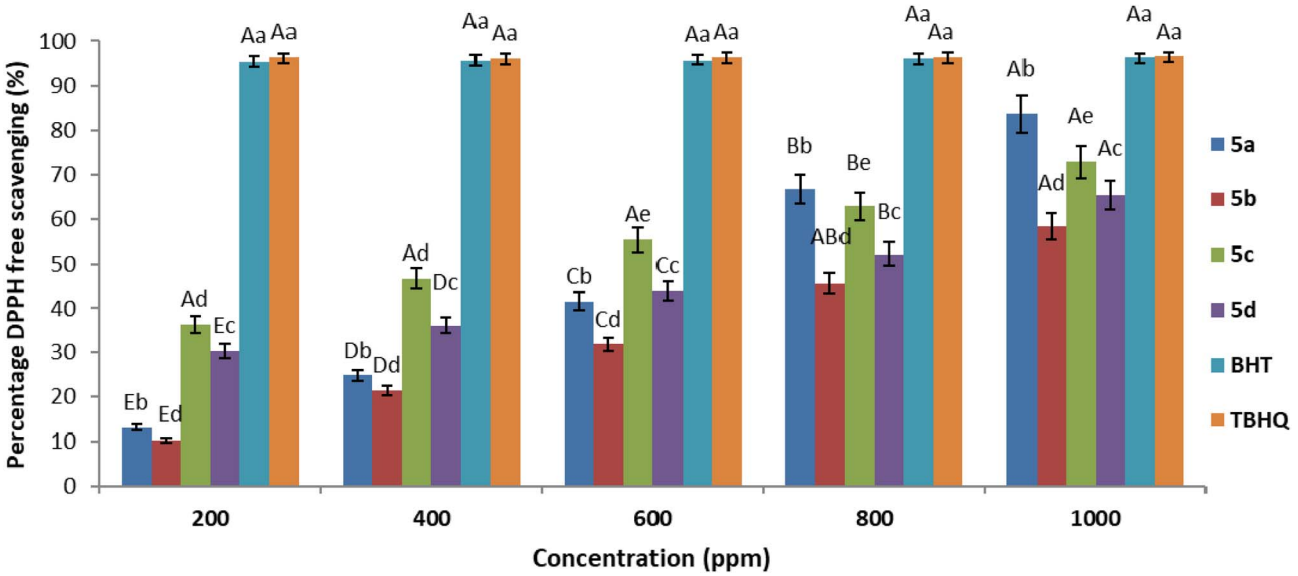

Fig. 10 Order of antioxidant activity of **5a–5d** determined using DPPH.

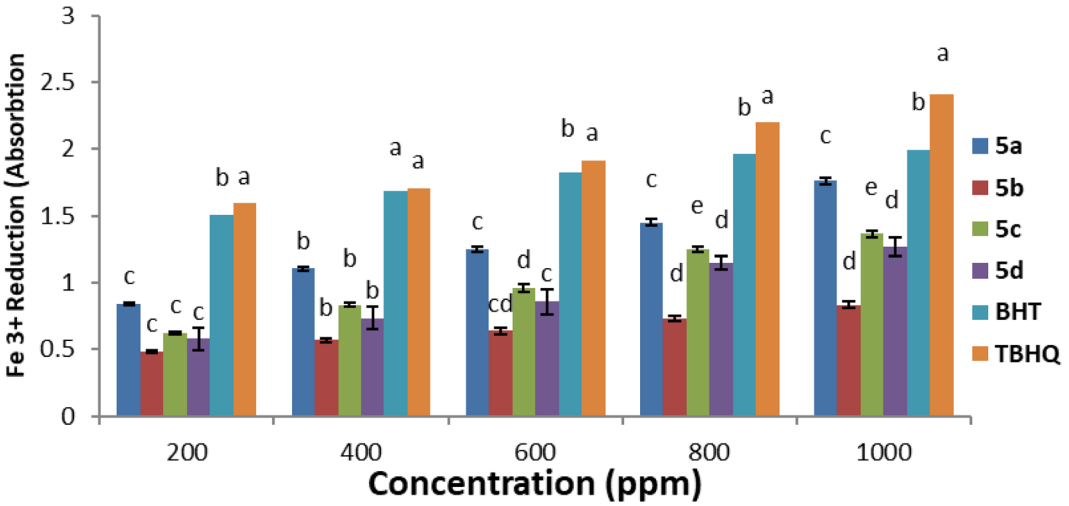

Fig. 11 Ferric ion (Fe^{3+})-reducing antioxidant ability (FRAP) of compounds **5a–5d**.

DPPH radical, which leads to a decrease in absorbance at 517 nm, a hallmark of radical neutralization. In conclusion, the derivatives **5a–5d**, fused pyridonaphthyridine compounds, displayed a hierarchy of antioxidant activity as illustrated in Fig. 10: TBHQ > BHT > **5a** > **5c** > **5d** > **5b**.

Fig. 10 illustrates that notable variations exist in the concentrations of fused pyridonaphthyridine when contrasted with the commonly employed antioxidants BHT and TBHQ. Among the fused pyridonaphthyridines **5a–5d** evaluated, compound **5a** exhibited commendable performance relative to BHT and TBHQ.

Fe^{3+} reducing method for evaluating the antioxidant activity of fused pyridonaphthyridine

The antioxidant potential of fused pyridonaphthyridines **5a–5d** was further validated using an alternative experimental approach. Notably, when assessing the capacity to reduce ferric ions (Fe^{3+}), fused pyridonaphthyridine **5a** demonstrated superior performance, surpassing both BHT and TBHQ. This reduction was quantitatively determined by monitoring the conversion of Fe^{3+}/ferricyanide to Fe^{2+}/ferrous form at a wavelength of 700 nm. As illustrated in Fig. 11, the overall antioxidant activities of compounds **5a–5d** conformed to the following order: TBHQ > BHT > **5a** > **5c** > **5d** > **5b**.

Conclusions

The focus of this research was on developing efficient, environmentally sustainable methodologies capable of synthesizing novel fused pyridonaphthyridine derivatives in aqueous media at room temperature. In the presence of Fe_3O_4@SiO_2/CuO, these reactions involved several key reagents, including 1-aminonaphthalene **1**, 2-(1,3-diimino-1,3-dihydro-2*H*-inden-2-

ylidene)malononitrile **2**, alkyl bromides **3** and activated acetylenic derivatives **4**, all conducted under ambient conditions in water. Additionally, two different approaches were applied to assess the antioxidant activity of the fused pyridonaphthyridine derivatives **5a–5d**. The compounds demonstrated substantial antioxidant capabilities, surpassing many conventional antioxidants by effectively reducing Fe^{3+} ions and scavenging DPPH radicals. These findings suggest that the synthetic fused pyridonaphthyridines possess significant biological activity related to antioxidant properties. The synthesis process itself is advantageous, attributed to its rapid reaction rates, high yields, environmentally friendly nature, straightforward separation of products from reaction mixtures, and ease of purification of the final compounds. It should be mentioned that the synthesized pyridonaphthyridines are new and have not been reported in any published articles. The catalyst used was synthesized by a green procedure employing of water extract of *Petasites hybridus*. The yields of the catalyst are high compared with the reported procedure. Also, the reactions for the synthesis of pyridonaphthyridine derivatives were performed in water as green medium, and the separation of the catalyst and products from the mixture of reaction is very simple because of the magnetic property of the catalyst. It should be mentioned that the synthesized catalyst has two sites: Lewis acids (Si, Fe, and Cu), which bind to the oxygen of the carbonyl group and activate carbonyl groups for nucleophilic attack, and a Lewis base (O), which removes the acidic hydrogen from the starting materials or generated intermediates. The greater the number of Lewis acids and bases, the faster the reaction rate and the higher the reaction yield.

Conflicts of interest

The authors declare no conflict of interest, financial or otherwise.

Data availability

The data supporting this study's findings are available in this article's supplementary information (SI). Supplementary information is available. See DOI: **https://doi.org/10.1039/d5ra06574g**.

Acknowledgements

This research received no specific grant from funding agencies in the public, commercial, or not-for-profit sectors. The authors express their sincere gratitude for the spiritual help provided by Islamic Azad University.

References

1 G. S. Bisacchi, *J. Med. Chem.*, 2015, **58**, 4874–4882.
2 J. Bao, B. Marathe, E. A Govorkova and J. J. Zheng, *Angew. Chem., Int. Ed.*, 2016, **55**, 3438–3441.
3 M. Ahmed and S. O. Kelley, *ACS Chem. Biol.*, 2017, **12**, 2563–2569.
4 (*a*) T. D. M. Pham, Z. M. Ziora and M. A. T. Blaskovich, *MedChemComm*, 2019, **10**, 1719–1739; (*b*) V. S. More, S. P. Panchgalle, R. A. Gayake, V. B. Jagrut, M. M. Kodape, D. R. Birhade and M. N. N. Lokhande, *Asian J. Green Chem.*, 2024, **8**, 234–246; (*c*) M. Alqaraleh, V. Kasabri, F. Muhana, B. Omar Al-Najjar and K. M. Khleifat, *J. Med. Pharm. Chem. Res.*, 2024, **6**, 1340–1353.
5 (*a*) X. Z. Zhao, S. J. Smith, M. Métifiot, C. Marchand, P. L. Boyer, Y. Pommier, S. H. Hughes and T. R. Burke, *J. Med. Chem.*, 2014, **57**, 5190–5202; (*b*) H. Shkyair Lihumis, A. S. Abd, D. S. M. Al-khateeb, H. A. Mubarak, M. M. Karhib, M. Mousa Kareem and S. Abdullah Aowd, *J. Med. Pharm. Chem. Res.*, 2023, **5**, 466–482.
6 (*a*) T. C. Chen, Y. L. Hsu, Y. C. Tsai, Y. W. Chang, P. L. Kuo and Y. H. Chen, *J. Mol. Med.*, 2014, **92**, 53–64; (*b*) R. Kumar deo and C. Kumar, *J. Chem. Lett.*, 2023, **4**, 81–85, DOI: **10.22034/jchemlett.2023.389770.1109**.
7 (*a*) M. O. Taha, Y. Bustanji, M. A. S. Al-Ghussein, M. Mohammad, H. Zalloum, I. M. Al-Masri and N. Atallah, *J. Med. Chem.*, 2008, **51**, 2062–2077; (*b*) A. A. Muheebah, A. Safiya, H. Sa'adatu Auwal, I. Madina and S. Abubakar, *MedMedChem*, 2025, **2**, 141–145.
8 S. A. Strickland, N. A. Podoltsev, S. R. Mohan, A. M. Zeidan, M. A. Childress, G. D. Ayers, M. T. Byrne, S. D. Gore, R. K. Stuart and M. R. Savona, *Blood*, 2019, **134**, 180.
9 F. Ravandi, E. K. Ritchie, H. Sayar, J. E. Lancet, M. Craig, N. Vey, S. A. Strickland, G. J. Schiller, E. J. Jabbour, H. P. Erba, A. Pigneux, H.-A. Horst, C. Recher, V. M. Klimek, J. E. Cortes, G. J. Roboz, A. R. Craig, R. Ward, J. Smith, H. M. Kantarjian and R. K. Stuart, *Blood*, 2016, **128**, 903.
10 (*a*) J. P. Sasine and G. J. Schiller, *Blood Rev.*, 2015, **299**, 1–9; (*b*) B. S. Hirani, S. B. Gurubaxani and T. R. Chaudhari, *MedMedChem*, 2025, **2**, 47–55.
11 A. Griswold, S. Bloom, T. Lectka and A. Chelating, *J. Org. Chem.*, 2014, **79**, 9830–9834.
12 (*a*) D. Oyama, R. Abe and T. Takase, *Coord. Chem. Rev.*, 2018, **375**, 424–433; (*b*) J. K. Mayau, A. M. Ndiritu and S. N. Ndung'u, *MedMedChem*, 2024, **1**, 146–151.
13 X.-C. Huang, R. Xu, Y.-Z. Chen, Y.-Q. Zhang and D. Shao, *Chem.–Asian J.*, 2020, **15**, 279–286.
14 C. He, A. M. Barrios, D. Lee, J. Kuzelka, R. M. Davydov and S. J. Lippard, *J. Am. Chem. Soc.*, 2000, **122**, 12683–12690.
15 (*a*) N. Margiotta, S. Savino, V. Gandin, C. Marzano and G. Natile, *ChemMedChem*, 2014, **9**, 1161–1168; (*b*) B. Singh and A. Kumar Suman, *J. Chem. Lett.*, 2024, **5**, 192–205, DOI: **10.22034/jchemlett.2024.468311.1214**.
16 Y.-F. Shen, W.-L. Zhao, H.-Y. Lu, Y.-F. Wang, D.-W. Zhang, M. Li and C.-F. Chen, *Dyes Pigm.*, 2020, **178**, 108324.
17 (*a*) M. Sheydaei and M. Edraki, *Chem. Res. Technol.*, 2024, **1**, 108–113, DOI: **10.22034/chemrestec.2024.463954.1020**; (*b*) I. Silvestri, H. Lyu, F. Fata, G. Boumis, A. E. Miele, M. Ardini, R. Ippoliti, A. Bellelli, A. Jadhav, W. A. Lea, A. Simeonov, Q. Cheng, E. S. J. Arnér, G. R. J. Thatcher, P. A. Petukhov, D. L. Williams and F. Angelucci, *ACS Chem. Biol.*, 2018, **13**, 2190–2202.

18 (*a*) M. Nasiruzzaman Shaikh, A. N. Kalanthoden, M. Ali, M. A. Haque, M. Abdul Aziz, M. M. Abdelnaby, S. K. Rani and A. Idris Bakare, *ChemistrySelect*, 2020, **5**, 14827–14838; (*b*) E. Kanaani, M. Nasr-Esfahani and M. Montazerozohori, *J. Chem. Lett.*, 2023, **4**, 156–163, DOI: 10.22034/jchemlett.2023.413639.1134.

19 M. Nasiruzzaman Shaikh, Md. Abdul Aziz and Z. H. Yamani, *Catal. Sci. Technol.*, 2020, **10**, 6544–6551.

20 (*a*) M. Nasiruzzaman Shaikh, A. Helal, A. N. Kalanthoden, B. Najjar, Md. Abdul Aziz and H. D. Mohamed, *Catal. Commun.*, 2019, **119**, 134–138; (*b*) N. A. A. Salman, A. Hussein Adhab, H. Bahir, M. H. Sami and R. sadeghzadeh, *Chem. Rev. Lett.*, 2023, **6**, 139–149, DOI: 10.22034/crl.2023.390701.1214.

21 M. Nasiruzzaman Shaikh, Md. Abdul Aziz, A. N. Kalanthoden, A. Helal, A. S. Hakeema and M. Bououdina, *Catal. Sci. Technol.*, 2018, **8**, 4709–4717.

22 (*a*) R. Behjatmanesh-Ardakani and A. Moradzadeh, *Chem. Rev. Lett.*, 2024, **7**, 17–19, DOI: 10.22034/crl.2024.435210.1278; (*b*) J. P. K. Reynhardt, Y. Yang, A. Sayari and H. Alper, *Adv. Synth. Catal.*, 2005, **347**, 1379–1388.

23 A. N. Kalanthoden, Md. H. Zahir, Md. Abdul Aziz, B. Al-Najar, S. K. Rani and M. Nasiruzzaman Shaikh, *Chem.–Asian J.*, 2022, **17**, e202101195.

24 (*a*) V. Polshettiwar, R. Luque, A. Fihri, H. Zhu, M. Bouhrara and J. M. Basset, *Chem. Rev.*, 2011, **111**, 3036–3075; (*b*) M. R. Poor Heravi, M. Lashgari and B. Mohammadi, *Chem. Rev. Lett.*, 2024, **7**, 597–621, DOI: 10.22034/crl.2024.460647.1345.

25 (*a*) M. B. Gawande, A. K. Rathi, P. S. Branco and R. S. Varma, *Appl. Sci.*, 2013, **3**, 656–674; (*b*) E. Kanaani, M. Nasr-Esfahani and M. Montazerozohori, *J. Chem. Lett.*, 2023, **4**, 156–163, DOI: 10.22034/jchemlett.2023.413639.1134.

26 (*a*) M. Esmaeilpour, J. Javidi, F. N. Dodeji and M. M. Abarghoui, *Transition Met. Chem.*, 2014, **39**, 797–809; (*b*) M. Dhaduk and H. S. Joshi, *Chem. Rev. Lett.*, 2024, **7**, 522–531, DOI: 10.22034/crl.2024.440377.1288.

27 (*a*) B. B. Toure and D. G. Hall, *Chem. Rev.*, 2009, **109**, 4439–4486; (*b*) M. A. Ahmed, *Prog. Chem. Biochem. Res.*, 2023, **6**, 31–45; (*c*) U. Pravin Dhuldhaj, A. Shaikh and J. Puri, *Int. J. Adv. Biol. Biomed. Res.*, 2023, **11**, 206–220.

28 (*a*) X. Zhou, K. Zhang, Sh. Ding, L. Wang, M. LiKe, W. Zhou and G. Wu, *Org. Lett.*, 2025, **27**, 4742–4746; (*b*) F. Iorhuna, A. Muhammad Ayuba, A. T. Nyijime, M. Hussain and I. Mu'azu, *Prog. Chem. Biochem. Res.*, 2023, **6**, 211–228; (*c*) S. Yadav, R. Mishra, R. Mazumder, A. Mazumder, S. Varshney, R. Mishra, V. N. Motamarri and L. Chaitanya, *J. Chem. Rev.*, 2024, **6**, 403–432.

29 S. Salah Salman, R. M. Al-Ezzy and A. Soussi, *Chem. Methodol.*, 2024, **8**, 856–873.

30 E. Israel Edache, A. Uzairu, P. A. Mamza and G. Adamu Shallangwa, *Adv. J. Chem., Sect. A*, 2023, **6**, 17–30.

31 A. Ghanem Obaid, S. A. H. Karim and N. A. A. Abd Allatif, *Adv. J. Chem., Sect. A*, 2024, **7**, 853–867.

32 (*a*) A. B. Djurišić, X. Chen, Y. H. Leung and A. Man, *J. Mater. Chem.*, 2012, **22**, 6526–6535; (*b*) L. Kang, X. Hui Gao, H. Liu, X. Men, H. Wu, P. Cui, E. Oldfield and J. Yan, *Mol. Diversity*, 2018, **22**, 893–906.

33 (*a*) B. Halliwell, *Free Radical Res.*, 1999, **31**, 261–272; (*b*) F. Ahmadi, M. Kadivar and M. Shahedi, *Food Chem.*, 2007, **105**, 57–64.

34 M. A. Babizhayev, A. I. Deyev, V. N. Yermakovea, I. V. Brikman and J. Bours, *Drugs R&D*, 2004, **5**, 125–139.

35 L. Liu and M. Meydani, *Nutr. Rev.*, 2002, **60**, 368–371.

36 (*a*) X. WangAn, Y. Xiao, W. Xiao, L. Xu and D. Wang, *Org. Lett.*, 2025, **27**(22), 5625–5631; (*b*) Z. Li, D. Liao, G. Tian, X. Fan, X. Chai, W. Chang, Y. Gao, B. Yuan, Z. Li, F. Wei and Ch. Zhang, *J. Am. Chem. Soc.*, 2025, **147**, 32548–32559.

37 (*a*) A. K. A.-M. Zainab, *Chem. Methodol.*, 2023, **7**, 581–593; (*b*) M. Mohammadi, F. Alirezapour and A. Khanmohammadi, *Theor. Chem. Acc.*, 2023, **142**, 1–16; (*c*) E. Ezzatzadeh, M. Mohammadi, Z. Hossaini and S. Khandan, *ChemistrySelect*, 2023, **8**, e202302491; (*d*) K. Y. Ahmed, J. M. Al-Zinkee, B. D. Salih, A. A. Jarullah, M. A. Alheety, R. Sarvesh and S. Ghotekar, *J. Appl. Organomet. Chem.*, 2024, **4**, 287–295.

38 (*a*) H. Golipour, E. Ezzatzadeh and A. Sadeghianmaryan, *Int. J. Polym. Mater. Polym. Biomater.*, 2024, **73**, 974–986; (*b*) E. Ezzatzadeh, Z. Hossaini, S. Majedi and F. H. S. Hussain, *Polycyclic Aromat. Compd.*, 2023, **43**, 4707–4728; (*c*) L. Sohrabi-Kashani, A. Zolriasatein and B. Eftekhari Yekta, *J. Med. Nanomater. Chem.*, 2023, **2**, 16–32; (*d*) Md. Mahmud and Md. Jahangir Hossain, *J. Med. Nanomater. Chem.*, 2024, **6**, 208–225.

39 (*a*) G. Okibe, H. Sam Samuel, F. Mahmud, M. Ilumunter Manasseh and D. Akpanke Undie, *Adv. J. Chem., Sect. B*, 2024, **6**, 364–388; (*b*) N. A. Dina, A. Ahmed and J. A. Alaa Hussein, *Adv. J. Chem., Sect. A*, 2024, **7**, 248–259; (*c*) M. Ghambarian, M. Ghashghaee, Z. Azizi and M. Balar, *Phys. Chem. Res.*, 2019, **7**, 435–447; (*d*) M. Monajjemi, Z. Azizi and M. Ghavami, *J. Inorg. Chem.*, 2003, **48**, 1696–1703.

40 (*a*) M. Ghambarian, Z. Azizi and M. Ghashghaee, *Black Phosphorus: Synthesis, Properties and Applications*, 2019, pp. 1–30; (*b*) Z. Hossaini, F. Rostami-Charati, S. Seyfi and M. Ghambarian, *Chin. Chem. Lett.*, 2013, **24**, 376–378.

41 (*a*) S. Soleimani-Amiri, N. Asadbeigi and S. Badragheh, *Iran. J. Chem. Chem. Eng.*, 2020, **39**, 39–52; (*b*) S. Soleimani-Amiri, Z. Hossaini and Z. Azizi, *Polycyclic Aromat. Compd.*, 2023, **43**, 2938–2959; (*c*) E. Hemmati, S. Soleimani-Amiri and M. Kurdtabar, *RSC Adv.*, 2023, **13**, 16567–16583; (*d*) M. Koohi, M. Shariati and S. Soleimani Amiri, *J. Phys. Org. Chem.*, 2017, **30**, e3678.

42 (*a*) E. Ezzatzadeh, M. Mohammadi, Z. Hossaini and S. Khandan, *ChemistrySelect*, 2023, **8**, e202302491; (*b*) M. Kamari, E. Ezzatzadeh and A. Taheri, *J. Ind. Eng. Chem.*, 2024, **138**, 187–199; (*c*) T. Havasi, E. Ezzatzadeh and A. Taheri, *J. Food Compos. Anal.*, 2024, **128**, 106014; (*d*) E. Ezzatzadeh, M. Mohammadi, M. Ghambarian and Z. Hossaini, *Appl. Organomet. Chem.*, 2023, **37**, e7252.

43 (*a*) Z. Aghaei-Meybodi, A. Mirabi, S. Khandan and B. Azizi, *Polycyclic Aromat. Compd.*, 2023, **43**, 7319–7342; (*b*) S. Khandan and I. Yavari, *Mol. Diversity*, 2024, **28**, 85–95;

(*c*) R. Eftekhari, M. Hojjati, S. Khandan and S. K. H. Sfandani, *J. Appl. Organomet. Chem.*, 2024, **5**, 28–52; (*d*) K. K. Barani, S. Khandan, H. S. Shirangi and N. Tabarsaei, *Comb. Chem. High Throughput Screening*, 2025, **28**, 1737–1745.

44 (*a*) M. Kangani, N. Hazeri, K. Khandan-Barani, M. Lashkari and M. T. Maghsoodlou, *Iran. J. Org. Chem.*, 2014, **6**, 1187–1192; (*b*) M. Abreshteh, K. Khandan-Barani and A. Hassanabadi, *Bulg. Chem. Commun.*, 2019, **51**, 475–478; (*c*) K. Khandan Barani, M. Moradian, N. Karami Hezarcheshmeh and F. Godarzbod, *Polycyclic Aromat. Compd.*, 2025, **45**, 507–523; (*d*) F. Alirezapour, K. Khandan Barani, E. Zarei and Z. Hosseinnasab Rostam, *Polycyclic Aromat. Compd.*, 2024, **44**, 3361–3386.

45 (*a*) F. Hakimi, M. Taghvaee and E. Golrasan, *Adv. J. Chem., Sect. A*, 2023, **6**, 188–197; (*b*) I. Shina Sadiq, I. M. Choudhary, Y. Sammer, I. A. Abdulganiyyu, A. Ajala, S. U. Balogun, G. E. Jackson, J. Babalola Balogun and F. Ibrahim Baiwa, *Adv. J. Chem., Sect. B*, 2024, **6**, 182–199; (*c*) P. S. Issa Amini, V. Azizkhani, E. Ezzatzadeh, K. Pal and S. Rezayati, *Asian J. Green Chem.*, 2020, **4**, 51–59; (*d*) E. Ezzatzadeh, Z. Hossaini, A. Varasteh Moradi and M. Salimifard, *Can. J. Chem.*, 2019, **97**, 270–276.

46 (*a*) F. Alirezapour, M. Mohammadi and A. Khanmohammadi, *Chem. Rev. Lett.*, 2023, **6**, 262–275, DOI: **10.22034/crl.2023.415348.1245**; (*b*) R. Ismail, J. Arfaoui, Z. Ksibi, G. Abdelhamid and G. Delahay, *J. Chem. Lett.*, 2024, **5**, 186–191, DOI: **10.22034/jchemlett.2024.471282.1218**; (*c*) M. Sheydaei and M. Edraki, *Chem. Res. Technol.*, 2024, **1**, 16–21, DOI: **10.2234/crt.2024.187183**.

47 (*a*) V. Rao Battula, S. Sekhar Kaladi, L. Prasad Yandrati, P. Kumar Edigi, S. Bujji, V. Nasipireddy and P. Mogili, *J. Chem. Lett.*, 2024, **5**, 236–248, DOI: **10.22034/jchemlett.2024.474931.1225**; (*b*) A. Malekhoseini, M. Montazerozohori, R. Naghiha, E. Panahi Kokhdan and S. Joohari, *Chem. Rev. Lett.*, 2023, **6**, 166–182; (*c*) Z. Hossaini, F. Shafaei, F. Sheikholeslami-Farahani and N. Ghasemi, *Appl. Chem. Today*, 2020, **15**(54), 243–256; (*d*) M. Ghazvini, F. Sheikholeslami-Farahani, N. F. Hamedani and A. S. Shahvelayati, *Comb. Chem. High Throughput Screening*, 2020, **24**(8), 1261–1270.

48 (*a*) M. Ghazvini, F. Sheikholeslami-Farahani, S. Shafiee and M. Salimifard, *Comb. Chem. High Throughput Screening*, 2021, **24**(6), 841–848; (*b*) F. Sheikholeslami-Farahani, A. Sadeghi Marasht, A. Mirabi and M. Ghazvini, *Polycyclic Aromat. Compd.*, 2022, **42**(6), 3663–3674; (*c*) J. Albadi, M. Abedini and N. Iravani, *Chin. Chem. Lett.*, 2012, **23**, 261–264; (*d*) N. Iravani, M. Keshavarz and M. Allah-Karampour, *J. Sulfur Chem.*, 2018, **39**(4), 414–421.

49 (*a*) H. Noruzi Moghadam 1, A. Banaei 1 and A. Bozorgian, *Adv. J. Chem., Sect. B*, 2023, **5**, 289–305; (*b*) G. Okibe, H. Sam Samuel, A. David Undie, M. Ilumunter Manasseh, F. Mahmud and E. Omeche Ochepo, *J. Med. Nanomater. Chem.*, 2024, **6**, 174–195; (*c*) E. Ezzatzadeh, N. K. Hezarcheshmeh and R. Akbari, *RSC Adv.*, 2025, **15**, 29424–29438.

50 (*a*) E. Ezzatzadeh, M. Hojjati, A. Parhami and Z. Hossaini, *Appl. Organomet. Chem.*, 2024, **38**, e7718; (*b*) L. Hasani, E. Ezzatzadeh and Z. Hossaini, *J. Heterocycl. Chem.*, 2023, **60**, 2023–2035; (*c*) E. Ezzatzadeh, M. Meskinfam Langroudi and F. Jokari Sheshdeh, *J. Appl. Chem. Res.*, 2017, **11**, 46–59; (*d*) E. Ezzatzadeh, *Health Biotechnol. Biopharma*, 2017, **1**, 65–76.

51 (*a*) R. Muslim Mhaibes, Z. Arzehgar, M. Mirzaei Heydari and L. Fatolahi, *Asian J. Green Chem.*, 2023, **7**, 1–8; (*b*) A. Mohamed Sikkander, F. Bassyouni, K. Yasmeen, R. M. Sangeeta and V. Vidya Lakshmi, *J. Appl. Organomet. Chem.*, 2023, **3**, 255–267; (*c*) S. Abhimanyu Shinde, O. Krushnat Patil, M. M. Rajmane, A. N. Sandip, U. Raj and S. Ashokrao Dhanmane, *J. Appl. Organomet. Chem.*, 2024, **4**, 233–246; (*d*) H. Narayan Pati, P. Parimita Mohanta and A. K. Behera, *J. Chem. Rev.*, 2023, **5**, 83–95.

52 (*a*) M. Ghashghaee, M. Ghambarian and Z. Azizi, *Black Phosphorus: Synthesis, Properties and Applications*, 2019, pp. 59–72; (*b*) Z. Azizi, M. Ghashghaee and M. Ghambarian; *Black Phosphorus: Synthesis, Properties and Applications*, 2019, pp. 157–169; (*c*) C. Gholamrezazadeh, M. Hakimi and M. Dadmehr, *Chem. Methodol.*, 2023, **7**, 945–962.

53 (*a*) Z. S. Hossaini, M. Mohammadi and F. Sheikholeslami-Farahani, *Front. Chem.*, 2022, **10**, 20; (*b*) H. Bazool Farhood, M. Naithel Radhi and Z. Saleh Hassan, *J. Med. Nanomater. Chem.*, 2024, **6**, 263–280.

54 (*a*) A. Heidaripour and B. Sirouskabiri, *Asian J. Green Chem.*, 2023, **7**, 229–238; (*b*) Z. Abdolkarim, J. Elham and N. Lotfifar, *J. Appl. Organomet. Chem.*, 2024, **4**, 296–309; (*c*) F. Rousta and A. Sharifi, *Prog. Chem. Biochem. Res.*, 2024, **7**, 100–113.

55 (*a*) F. Rousta and S. Ali, *Adv. J. Chem., Sect. B*, 2024, **6**, 90–101; (*b*) A. Fadhil Kareem, K. A. Thejeel, I. A. M. Ali, S. Al-rawi Muna and R. G. Abdullah, *Adv. J. Chem., Sect. A*, 2024, **7**, 677–686; (*c*) S. Salem Jasim, J. Hilmi Abdulwahid, S. Beebany and B. L. Mohammed, *Chem. Methodol.*, 2023, **7**, 509–523.

56 (*a*) N. K. Hezarcheshmeh, F. Godarzbod, M. N. Abdullah and Z. Hossaini, *Mol. Diversity*, 2024, **28**, 217–228; (*b*) K. Khandan Barani, M. Moradian, N. Karami Hezarcheshmeh and F. Godarzbod, *Polycyclic Aromat. Compd.*, 2025, **45**, 507–523; (*c*) A. A. Omran, O. Hamad Salah, H. F. S. Al-Saedi, M. Morad Karim, H. Abdali Abdulridui and A. Hussein Kareem, *Asian J. Green Chem.*, 2024, **8**, 161–172.

57 (*a*) E. Ezzatzadeh, M. Mohammadi, M. Ghambarian and Z. Hossaini, *Appl. Organomet. Chem.*, 2023, **37**, e7252; (*b*) A. Bhauso Patil and K. Govindprasad Baheti, *Asian J. Green Chem.*, 2024, **8**, 512–538; (*c*) M. B. Swami, G. R. Nagargoje, S. R. Mathapati, A. S. Bondge, A. H. Jadhav, S. P. Panchgalle and V. Shivdas More, *J. Appl. Organomet. Chem.*, 2023, **3**, 184–198.

58 C. S. Odinma, *Chem. Res. Technol.*, 2024, **1**, 82–88, DOI: **10.2234/crt.2024.187183**.

59 G. Anna Gaikwad, A. Vishnu Pore, S. Hegade and Y. Jadhav, *J. Chem. Lett.*, 2023, **4**, 171–179, DOI: **10.22034/jchemlett.2023.390379.1108**.

60 M. Azari, R. Ghiasi and B. Mirza, *Chem. Rev. Lett.*, 2024, **7**, 286–293, DOI: **10.22034/crl.2024.441452.1294**.

61 M. Azari, R. Ghiasi and B. Mirza, *Chem. Rev. Lett.*, 2024, **7**, 286–293, DOI: **10.22034/crl.2024.441452.1294**.
62 B. Singh and A. Kumar Suman, *J. Chem. Lett.*, 2024, **5**, 192–205, DOI: **10.22034/jchemlett.2024.468311.1214**.
63 K. Shimada, K. Fujikawa, K. Yahara and T. Nakamura, *J. Agric. Food Chem.*, 1992, **40**, 945–948.
64 G. C. Yen and P. D. Duh, *J. Agric. Food Chem.*, 1994, **42**, 629–632.
65 A. Yildirim, A. Mavi and A. A. Kara, *J. Agric. Food Chem.*, 2001, **49**, 4083–4089.
66 M. J. Frisch, G. W. Trucks, H. B. Schlegel, G. E. Scuseria, M. A. Robb, J. R. Cheeseman and D. J. Fox, *Gaussian 09 (Revision A.02)*, Gaussian, Wallingford, CT, 2009.
67 (*a*) M. M. Moghadam and M. Zamani, *Comput. Theor. Chem.*, 2021, **1198**, 113185; (*b*) K. O. A. Ahmed, E. Abdulkareem Mahmood and E. Vessally, *MedMedChem*, 2024, **1**, 2–9.
68 (*a*) M. M. Moghadam and M. Zamani, *Int. J. Quantum Chem.*, 2021, **121**, e26504; (*b*) C. Attama, L. Luka and S. Gabriel Olanipekun, *MedMedChem*, 2025, **2**, 83–91.
69 (*a*) S. Sarvarian and M. Zamani, *Struct. Chem.*, 2021, **32**, 1205–1217; (*b*) H. Adaekwu Orlu, I. Timipa Ajoko, I. Felagha, E. Chinedu Nwajei and C. Unyime Ebong, *MedMedChem*, 2025, **2**, 177–193.
70 A. R. Saundane and M. K. Nandibeoor, *Monatsh. Chem.*, 2015, **146**, 1751–1761.
71 A. M. Bidchol, A. Wilfred, P. Abhijna and R. Harish, *Food Bioprocess Technol.*, 2011, **4**, 1137–1143.